THESIS APPROVAL

The abstract and thesis of Christy L. Lee for the Master of Science in Geology presented November 9, 2000, and accepted by the thesis committee and the department.

COMMITTEE APPROVALS:

Michael L. Cummings, Chair

Kenneth M. Cruikshank

Martin J. Streck

Virginia L. Butler
Representative of the Office of Graduate Studies

DEPARTMENTAL APPROVAL:

Ansel G. Johnson, Chair
Department of Geology

Abstract

An abstract of the thesis of Christy L. Lee for the Master of Science in Geology presented November 9, 2000.

Title: Magmatic processes operating during the middle to late Pliocene and Pleistocene along the Cascades - Basin and Range transition zone near 43º North.

A geochemical and structural transition zone exists between the Cascades and Basin and Range provinces in Oregon. Geologic mapping in this area has allowed the definition of six volcanic rock sequences: 1) interfingered alkali-rich basaltic trachyandesite to trachydacite lava flows and low-alkali basaltic andesite lava flows, 2) HAOT lava flows, 3) basaltic andesite lava flows, 4) andesite lava flows and vent deposits with minor basaltic andesite lava flows, 5) HAB lava flows, and 6) interfingered basaltic andesite, andesite, and trachyandesite lava flows.

Geochemical models of sequence 1 alkali-rich rocks suggest the fractionation of the parent assemblage plag (An_{55})+magn+ol±aug at relatively dry (H_2O < 0.4 weight percent) and shallow (P = 1.5 to 3 kbar (< 9 km)) initial conditions. As water content increases, augite and olivine disappear to form the daughter assemblage plag (An_{29})+opx+magn+amph+ap. Approximately 50 percent fractionation combined with contamination by a LIL and LREE enriched and HFSE and HREE depleted contaminant account for the observed geochemical trends in these rocks.

Sequence 2 HAOT have similar geochemistry to N-MORB and are LIL, HFSE, LREE and incompatible element enriched when compared to the composition of

primitive mantle. In addition, sequence 2 HAOT geochemical trends are more similar to HAOT erupted along the Cascades than HAOT from the Basin and Range.

Andesitic lavas of sequences 1 (low-alkali), 3, 4, and 6 show evidence of batch melting and mixing in their scatter on geochemical diagrams and in their textures (e.g., complex plagioclase zoning patterns, abundant inclusions in plagioclase phenocrysts, and multiple plagioclase phenocryst populations).

The variety of lava types produced reflect multiple magmatic processes that may be distinctive of the Cascades - Basin and Range transition zone. HAOT and HAB lavas were able to rise to the surface with little to no ponding in the crust. Magmas were able to rise to shallow levels where they underwent fractionation and contamination to produce alkali-rich trachytic suites. Multiple andesitic lavas are most likely the product of batch melting and combined fractionation, contamination and magma mixing. These sequences are consistent with extension in the transition zone during the middle to late Pliocene and Pleistocene.

MAGMATIC PROCESSES OPERATING DURING THE MIDDLE TO LATE PLIOCENE AND PLEISTOCENE ALONG THE CASCADES - BASIN AND RANGE TRANSITION ZONE NEAR 43º NORTH

by

CHRISTY L. LEE

A thesis submitted in partial fulfillment of the
requirements for the degree of

MASTER OF SCIENCE
in
GEOLOGY

Portland State University
2000

Acknowledgments

Funding for this study was provided by the U.S. Geological Survey Educational Mapping Program Award Number 98HQAG2102 and the Oregon Department of Geology and Mineral Industries (DOGAMI).

This project would never have reached completion without the advice and support of several individuals. Because there are so many, I have chosen to expand on only three people here. I would like to acknowledge my advisor Mike Cummings for the hours of advising during scheduled meetings or just passing in the hall. He taught me that one must produce *something* before it can be revised. I would also like to acknowledge Martin Streck for his superior teaching skills. I owe much of my knowledge of petrology to his teachings. Finally, I would like to acknowledge my husband, Thomas Confar, who financially supported me and pushed me to complete this project.

I would also like to commend the PSU geology department faculty. I not only leave this school with a much increased knowledge of geology, I also leave with a better sense of myself as a geologist. I now feel that I may converse on an intelligent level with other geologists whether they are in the academic or the professional realm.

Others who played a role in the mapping project associated with this study are Robin Johnston (PSU), Ken Cruikshank (PSU), David Percy (PSU), Jeff Conaway (PSU), Charlie Palmer (PSU), Tom Wiley and George Priest (DOGAMI), Andy Peavy and Jim Dorr (Winema National Forest), W. P. Layer at the University of Alaska, Fairbanks, Dave Sherrod (USGS), and the rangers of Collier State Park.

Table of Contents

List of Tables

Number *Page*

List of Figures

Number *Page*

Introduction

The geochemical and structural transition between the Cascade volcanic province and the Basin and Range province has been studied by Guffanti and Weaver (1988), Carlson and Hart (1990), Hermance (1990), Dzurisin et al. (1990), Grose et al. (1990), Catchings (1990), and Pezzopane and Weldon (1993). While most studies have concentrated on the tectonic implications of the zone of transition, Carlson and Hart (1990) described temporal and spatial relations of calc-alkalic and tholeiitic volcanism. From approximately 17 Ma to 10.5 Ma, Carlson and Hart (1990) indicate a westward migration of tholeiitic volcanism through areas previously characterized by calc-alkalic volcanism. Because calc-alkalic volcanism is often associated with convergent margins, and likewise, tholeiitic volcanism may be associated with continental rifting (extensional terrains), the westward migration of the calc-alkalic-tholeiitic boundary is hypothesized to reflect a change in lithospheric thickness coupled with changing compressional orientations. These conditions may determine the transit time of magmas passing through the lithosphere.

Although a zone of transition has been studied by the workers listed above, it has generally been viewed as a structural transition, or a change in lithospheric thickness. Hart and Carlson (1990) first described the transition zone in terms of a geochemical change, but they were interested in a migration of geochemical change. This paper is concerned with the recognition and characterization of the transition zone in terms of a geochemical change. Specifically, this paper will identify the

magmatic processes that operated between the Cascades and Basin and Range provinces near 43º N during the middle to late Pliocene and Pleistocene.

Geologic mapping in the Soloman Butte (Lee and Cummings, in review) and Wocus Bay (Conaway and Cummings, in press) quadrangles defined stratigraphy and geochronology of volcanic rocks in a 15 km wide area believed to lie within the Cascades - Basin and Range transition zone near 43º N. The stratigraphic relationships, geochronology, and geochemistry of the volcanic units provide the basis for identification of the magmatic processes that operated during the middle to late Pliocene and Pleistocene in this area.

In this report, the geology, petrographic descriptions, and geochemical characteristics of the lavas in the study area are presented. Geochemical modeling based on major and trace element geochemistry is used to identify the magmatic processes involved in the petrogenesis of selected volcanic sequences. Finally, magmatism in this portion of the transition zone is discussed.

Analytical Methods

X-ray fluorescence data were produced by the GeoAnalytical Laboratory at Washington State University for samples located in the Soloman Butte quadrangle and prepared by the author (**Error! Reference source not found.**). Results are reported on a volatile-free basis and calculated with total iron expressed as FeO (FeO*). X-ray fluorescence and INAA geochemical data for all samples that comprise sequences 1, 3, and 5 and sample numbers 14, 19, 22, 24, Ws38, 53, 55, and 57 of sequence 4 were obtained from Conaway and Cummings (in press).

Geochemical data for sample number 52 (sequence 6) (**Error! Reference source not found.**) were obtained from unpublished data of George Priest (11/28/98, personal communication). Geochemical data for sample number 31 (sequence 6) were obtained from Tom Wiley (Wiley, in press). Instrumental neutron activation analysis (INAA) was conducted at Portland State University by the author for samples that comprise sequences 2, 4, and 6 (Appendix B) after irradiation at the Reed Reactor Facility, Portland, Oregon. Samples were irradiated for 1 hour at approximately 250 kw. Samples were transferred to Portland State University within 4 days of irradiation and first counts were conducted starting five days after irradiation. First counts were for 1500 seconds and second counts (14 days after irradiation) were for 3000 seconds. Analytical results for standards used in data analysis are reported in Appendix B. It is important to note that the INAA results are subject to analytical error; the reader is encouraged to check the results of the standards against their known concentrations. For example, the known concentration of Sc in the JA-2 standard is 19 ppm, while the analytical result is 18.37 ppm. Likewise, the known concentration of Sc in the JGb-1 standard is 35 ppm, while the analytical result is 34.03, and the known concentration of Sc in the JR-1 standard is 5.2 ppm, while the analytical result is 4.48 ppm. All XRF samples and selected INAA samples have accompanying thin sections, which have been analyzed using standard petrographic techniques. Petrographic descriptions and photomicrographs are included in Appendix C.

Age determinations (Conaway and Cummings, in press) for whole rock samples were performed using the $^{40}Ar/^{39}Ar$ method and results are reported in Table 2. Six age determinations were performed by P. W. Layer at the Geochronological Laboratory at the University of Alaska, Fairbanks (**Error! Reference source not found.**) (Conaway, 2000). One $^{40}Ar/^{39}Ar$ age determination was obtained from unpublished data of George Priest (11/28/98, personal communication).

Geology

Regional Geology

Oregon is the site of active subduction along the Cascadia subduction zone, and active extension in the back-arc and Basin and Range province. Abundant and diverse volcanic rocks have been produced through time in this tectonically active region. The following discussion describes the transitional area between the Cascade Mountains and Basin and Range physiographic provinces in terms of location, age and geology (Figure 1). The geochemical and petrologic trends and the magmatic processes acting to produce these rocks will be outlined in the petrology section.

High Cascades magmatic province

The Quaternary composite volcanoes of the north-trending Cascades volcanic arc lie to the west of the study area. The composite volcanoes of the High Cascades extend from Mt. Lassen in northern California to Mt. Garibaldi in southern British Columbia and, in Oregon, are built on Plio-Pleistocene basalt and basaltic andesite shield volcanoes of the older Cascade arc. Rocks of the High Cascades that crop out just west of the study area are composed primarily of 3.5 - 0 Ma basalt, basaltic

andesite and andesite. These rocks are calc-alkalic series lavas that have volumetric proportions near 30 percent basalt, 35 percent basaltic andesite and 35 percent andesite to rhyodacite (Sherrod, 1988). Volcanic rocks in this province are the product of magma genesis between the subducting oceanic slab and overlying continental plate (i.e., the mantle wedge). In this scenario, metamorphism of the subducted material (oceanic crust and overlying sediments) may cause fluids to transport these geochemical signatures into the mantle wedge (Peacock and Leeman, 1994) where metasomatism may occur (Conrey et al., 1997). As magmas rise into lower crustal levels, the combined magmatic processes of fractionation, magma mixing, and crustal assimilation most likely produce the erupted lavas along the arc (Brikowski, 1983; Sherrod, 1988; Bacon et al., 1997).

Crater Lake lies approximately 80 km west of the study area. The ancestral Mount Mazama is an andesitic composite volcano of the High Cascades. Its proximity to the study area and geochemistry of the volcanic products warrant discussion here. Multiple basaltic to andesitic cinder cones and rhyodacitic domes surround the volcano. The geochemical patterns discussed in Prueher and McBirney (1988) of the high-alumina basaltic to andesitic lavas associated with the cinder cones indicate that combined fractionation and magma mixing produced the lavas.

In these rocks, strong positive europium anomalies observed on rare earth element (REE) diagrams are inconsistent with plagioclase fractionation in the fractionating assemblage olivine, plagioclase, clinopyroxene, orthopyroxene, and magnetite. Prueher and McBirney (1988) conclude that the addition of plagioclase to

the magma occurred during magma mixing events producing the positive europium anomalies. Magma mixing is supported by petrographic textural evidence (e.g., abundant inclusions and complex zoning patterns in plagioclase phenocrysts). Subsequent fractionation of the mixed magmas is supported by stronger light REE (LREE) enrichment patterns in successive basalt to andesite sequences. In addition, the variation in geochemical patterns of cinder cone lavas can be explained by the injection of geochemically distinct batches of primary magma produced by discrete partial melting events of mantle peridotite.

Northern Basin and Range magmatic province

The northern Basin and Range province lies to the east and is characterized by north-northwest trending normal fault-bounded blocks. The Basin and Range province terminates in the High Lava Plains along the Brothers Fault Zone, and is underlain by rhyolite volcanic centers and relatively primitive, high-alumina Plio-Pleistocene to Holocene basalt (Draper, 1991). These primitive basalts are found throughout the northern Basin and Range province and at least as far east as Steens Mountain (Gunn and Watkins, 1970; McKee et al,. 1983; Hart et al., 1984). The primitive basalts erupted in the northern Basin and Range and in the Devil's Garden lava field (following section) bear the geochemical signature of a shallow homogeneous oceanic mantle source with little to no contamination by crustal material (Bullen, 1983; McKee et al., 1983; Draper, 1991; Bailey and Conrey, 1992).

Devil's Garden lava field

The Devil's Garden lava field is located between 41º30' and 43º N and 121º30' and 120º30' W in the northern Basin and Range province in northeastern California

and south central Oregon (Figure 1). This area is part of the region called the Modoc Plateau (MacDonald, 1966) and is locally recognized as the Devil's Garden. The proximity to the study area and composition of the lavas warrant discussion here. The geology and geochemistry of the Devil's Garden lava field are described in McKee et al. (1983), Bullen (1983, 1984, 1986), and Sawlan and Russell (1991). More comprehensive discussions on the geology of the Modoc Plateau can be found in McKee and Duffield (1979), Kramer (1980), England (1987), Miller (1988), Montgomery (1988), De La Fuente and Tatman (1991), Bolton et al. (1997), and Lavine and Aalto (1997).

The Devil's Garden lava field is comprised of a relatively coherent sequence of high-alumina basalt lavas (HAB) that are late Miocene to early Pliocene age. To the west, some of these lavas are conformably overlain by younger volcanic rocks in the Medicine Lake and Klamath Falls areas. These lavas are dominantly diktytaxitic olivine tholeiites cut by north-northwest-striking normal faults of the Basin and Range. The basalt of Devil's Garden unconformably overlies tuffaceous and lacustrine sedimentary rocks.

Bullen (1983) described the HAB's as not depleted in compatible elements, large ion lithophile element (LIL) depleted, and with highly variable concentrations of incompatible elements. He concluded that this compositonal diversity of the Devil's Garden magmas was produced by fractionation and by partial melting of a homogeneous source. He also concluded that the HAB's were generated in a mantle undergoing metasomatism.

In contrast to Bullen's (1983) conclusions, McKee et al. (1983) concluded that the Devil's Garden HAB's were not contaminated by crustal material, but rather originated in the upper mantle and were erupted through thinned crust that had undergone rapid extension during the Miocene and Pliocene.

Volcanics of the Cascades-Basin and Range transition zone

The following discussion outlines the geology and location of the volcanic rocks that lie between the High Cascades and the Basin and Range. These volcanics include the Yamsay Mountain volcanic complex, Newberry Volcano, and Medicine Lake Volcano.

Yamsay Mountain volcanic complex

The Yamsay Mountain volcanic complex is located near 43º N and 121º15' W along the boundary between Klamath and Lake counties Figure 1). The geology and petrology of the Yamsay Mountain volcanic complex are described in Hering (1981).

There are three main centers that comprise the Pliocene (4.79 ± 0.17 Ma) calc-alkalic Yamsay Mountain volcanic complex: Rodman Rock, Booth Ridge and Yamsay Mountain. Basaltic andesite was erupted from all three centers. The rocks of the complex are divided into four stages based on geologic association and order of eruption. Stage 1 includes two rhyolitic obsidian-rich domes, and stage 1 products consist of porphyritic basaltic andesite shield lavas and porphyritic rhyolitic lavas. Stage 2 rocks consist of a crystal-lithic welded tuff with well-developed eutaxitic texture. Stage 3 rocks are composed of dacite erupted from circumferential fractures near the top of the shield (beginning of caldera development) and aphyric basaltic andesite erupted from volcanoes built along the caldera rim. Stage 4 products consist

of porphyritic basaltic andesite erupted from the three centers and dacite erupted before and after the porphyritic basaltic andesite.

Hering (1981) concludes that discrete partial melting events were responsible for the production of the compositionally diverse basaltic andesite lavas at Yamsay Mountain volcanic complex, and differentiation of a dacitic parental magma produced the silicic lavas. Furthermore, this dacitic parent may have been produced in a compositionally zoned magma chamber beneath Yamsay Mountain where crystallization along the walls allowed the fractionated liquid to rise. Hering concludes that the silicic rocks at Yamsay Mountain volcanic complex formed by the melting of crustal rocks of basaltic composition.

Newberry Volcano

Newberry Volcano is located about 60 km east of the High Cascades near 44º N and between 121º and 122º W (Figure 1). The volcano is located at the west end of the High Lava Plains physiographic province and is one of the largest Quaternary volcanoes in the coterminous United States. The geology, eruptive history and geochemistry are described in Higgins (1968, 1973), Beyer (1973), Sherrod and MacLeod (1979), MacLeod et al. (1982), MacLeod and Sherrod (1985, 1988), Jensen (1988), Keith and Bargar (1988), Linneman (1990), Lambert and Goles (1992), MacLeod et al. (1995), and Gardner et al. (1998).

Newberry Volcano is comprised of a shield volcano with a 7 km diameter caldera, numerous basaltic cinder cones and silicic lava domes surrounded by Cenozoic volcanic and volcaniclastic sedimentary rocks. Much of Newberry Volcano's activity occurred within the last 0.5 million years, including caldera

collapse, caldera-filling volcanism and multiple Plinian eruptions. Newberry Volcano has erupted at least 25 times during the Holocene with the most recent eruption 1300 years ago.

A sequence of pyroclastic-flow and fall out tuffs, alluvial deposits and minor basalt lava flows (including high-alumina olivine tholeiite, HAOT) comprise the oldest strata exposed on the east and west flanks of the volcano. The north and south flanks are underlain by calc-alkalic porphyritic basaltic andesite with subordinate basalt and andesite lava flows whose ages are poorly defined. Basaltic cinder cones are abundant on the lower north and south flanks, but are also present on the upper flanks of the volcano. Dacite, rhyodacite and rhyolite lava domes are present on the middle and upper flanks and inside the caldera. The summit caldera is a collapse structure surrounded by several ring fractures. Pleistocene and Holocene lava flows, pyroclastic rocks and domes partially fill the caldera. The Pleistocene lavas are progressively more mafic down section from rhyodacite to basalt. Other Pleistocene rocks consist of an obsidian flow, a rhyodacite sill and basaltic and rhyolitic lapilli tuff.

Holocene volcanic rocks were produced during six eruptive episodes: four rhyolitic and two basaltic. The product of the first episode predates the 7,627±150 cal. yr. B. P. (Zdanowicz et al., 1999) cataclysmic eruption of Mount Mazama and consists of an obsidian flow with an associated dome. The second episode is also pre-Mazama and its products consist of mafic cinder, scoria and spatter erupted on the east rim of the caldera. The products of the third episode are comprised of rhyolitic

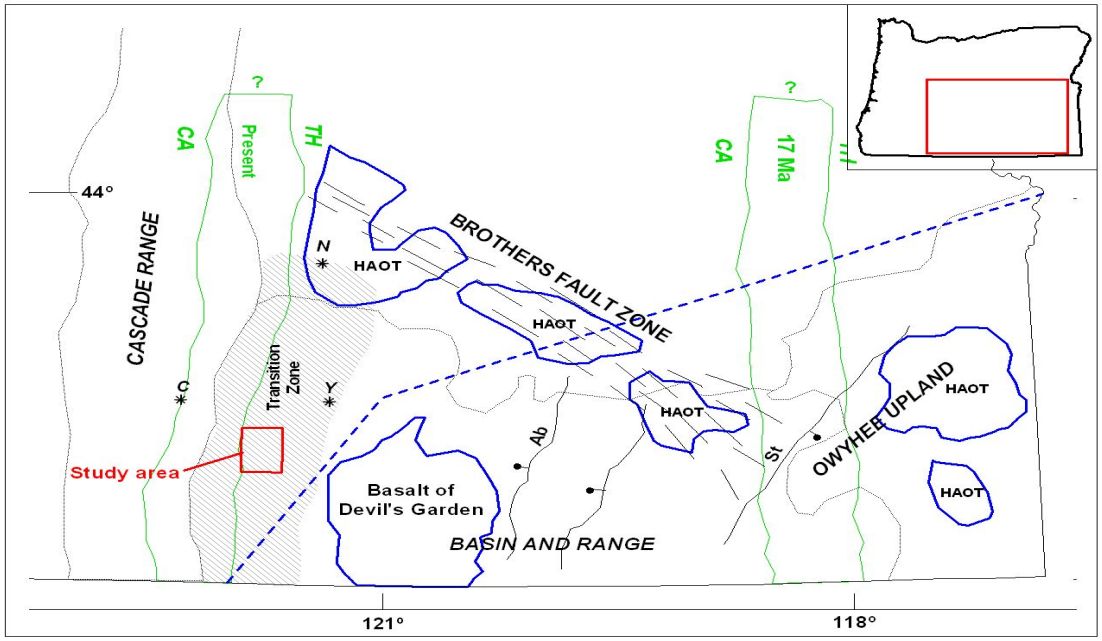

Figure 1: Physiographic provinces with pertinent fault zones and lavas in southern Oregon. Superimposed solid blue lines outline the extent of high-alumina olivine tholeiite (HAOT) as discussed in Draper (1991) and McKee et al. (1983). Dashed blue line outlines the extent of HAOT as discussed in Hart et al. (1984). Green lines denote the change from calc-alkaline to tholeiitic series lavas at 17 Ma and 10.5 Ma to present after Carlson and Hart (1990). Gray shaded area depicts the Casca.des - Basin and Range transition zone as interpreted by this study. Ab=Abert Rim and St=Steens Mountain, C=Crater Lake, N=Newberry Volcano, Y=Yamsay Mountain. Medicine Lake Volcano lies just south of the Oregon border in northern California near 41º N and 121º W.

eruptions within the caldera following the cataclysmic eruption of Mount Mazama. Basaltic andesite cinder cones, fissure vents and lava flows are associated with the fourth episode. Episode five products are comprised of obsidian flows and pumice deposits. Finally, episode six is marked by Plinian eruption deposits of tephra, ash-flow and an obsidian flow.

Higgins (1973) first discussed the petrology of Newberry Volcano in terms of differentiation trends developed before and after the formation of the caldera lake. He concluded that pre-caldera lake rocks followed a tholeiitic trend, while post-caldera lake rocks followed a calc-alkalic trend. MacLeod and Sherrod (1988) concluded that a rhyolitic magma chamber has existed below Newberry for most of the Holocene and that it has undergone intermittent underplating by basaltic magma. Silicic inclusions in basaltic andesite suggests magma mixing of basaltic and rhyolitic liquids.

Linneman (1990) examined the possibility of crustal melting associated with repeated mafic magma injections to produce the basalt-rhyolite suite at Newberry Volcano. He further concludes that single magmatic processes alone (e.g., fractional crystallization, assimilation, two component mixing) cannot account for the suite of Newberry volcanics.

Medicine Lake Volcano

Medicine Lake Volcano is part of the Modoc Plateau (as discussed in the *Devil's Garden lava field* section). It is located in northern California just east of the main axis of the Cascades between 41 and 42º N and 121 and 122º W (Figure 1).

Medicine Lake Volcano is a shield that rises approximately 1200 m above the Modoc Plateau (elevation 2376 m). The geology and petrology of Medicine Lake Volcano are discussed in Mertzman (1977), Gerlach et al. (1981), Grove et al. (1981,1982), Gerlach and Grove (1982), Grove et al. (1983), Grove and Baker (1984), Grove and Donnelly-Nolan (1986), Wood and Kienle (1990), Donnelly-Nolan (1990), Dzurisin et al. (1990), and Sisson and Grove (1993).

The geology of Medicine Lake Volcano can be generalized into three stages: early shield-forming stage, pre-caldera and caldera-forming stage, and post-caldera stage. The shield that forms Medicine Lake Volcano began to grow approximately one million years ago. The oldest flows consist of Pleistocene to Holocene tholeiitic, low-K high-alumina basalt (HAOT) and andesite. Similar high-alumina basalt has continued to erupt throughout its history and lavas ranging from basalt to rhyolite have also erupted during the Pleistocene. While HAOT lavas dominate the lower flanks, andesite with minor rhyolite and rare dacite are present at higher elevations; basalt is nearly absent. During this stage of caldera formation, Donnelly-Nolan (1988) concluded that the caldera formed by collapse in response to repeated extrusions of mafic lavas.

Much of the activity at Medicine Lake Volcano has occurred within the past 11,000 years after caldera formation. Eruptions have been episodic with eight basaltic eruptions around 10,500 years B. P., and a small andesite eruption about 4,300 years B.P. In the late Holocene, nine eruptions during a 3,400 year interval produced basalt to rhyolite lavas. The most recent eruption occurred 900 years ago

and produced basalt, rhyolite and dacite. The andesites and more silicic lavas are thought to have been produced through the combined processes of fractionation, assimilation and mixing (Grove et al., 1982).

Geology of the study area

Location

The study area is comprised of two 7.5 minute USGS quadrangles located between 42º37'30" and 42º52'30" N and 121º52'30" and 121º37'30" W in Klamath County, Oregon (Figures 2 and 3). Upper Klamath Lake and Agency Lake lie just southwest, Crater Lake National Park (ancestral Mount Mazama) lies to the west, and the southern extent of Klamath Marsh lies within the northern part of the map area.

Geologic Framework

Previous work in the study area is limited to reconnaissance studies which include a geomorphological study of Klamath Marsh by Williams (1942), groundwater studies by Meyers and Newcomb (1952), Illian (1970) and Leonard and Harris (1974) and a mineral resource investigation by Peterson and McIntyre (1970). One early geologic study by Merewether (1953) details the structure and stratigraphy of the eastern half of the Soloman Butte quadrangle between 121º48'12"W and 121º52'30"W. The oldest rocks described are a series of Pliocene interbedded pyroclastic rocks, basalt cinder cones, and tuffaceous sedimentary rocks and diatomite. The sedimentary rocks are overlain by Plio-Pleistocene coarse-grained basaltic tuff, breccia and agglomerates of variable thickness that crop out as remnants of tuff and cinder cones. The most widespread unit consists of a series of Plio-Pleistocene olivine basalt, basalt and andesite lava flows. These rocks are massive

lava flows, pillow lavas and flow breccia. North- and northwest-striking normal faults with dip-slip displacement up to 150 m cut the Plio-Pleistocene lavas.

Recent work in the study area is limited to two small-scale geologic maps: Walker and MacLeod's (1991) *Geologic Map of Oregon* (scale 1:500,000) and Sherrod and Pickthorn's 1992 *Geologic map of the west half of the Klamath Falls 1° by 2° quadrangle* (scale 1:250,000). Sherrod and Pickthorn (1992) indicate that the study area is dominated by Pliocene to Pleistocene effusive basalt and basaltic andesite lava flows and related vent deposits. These lava flows are underlain by Pliocene hydrovolcanic and sedimentary deposits to the south. Pyroclastic-flow and fall out deposits from the 7,627 ± 150 cal. yr. B. P. (Zdanowicz et al., 1999) cataclysmic eruption of Mount Mazama dominate the surficial units. North-northwest striking normal faults cut all bedrock units and have displacements greater than 100 m.

Young (1990) summarizes the Holocene airfall deposits from Mount Mazama, which dominate surface deposits in the study area. Young's "climactic pumice fall" is made up of a complex internal stratigraphy that consists of a basal ash bed, a lower pumice unit, an ash bed and an upper pumice unit. These units are further subdivided into proximal, medial and distal sections; the study area is primarily located within the medial section.

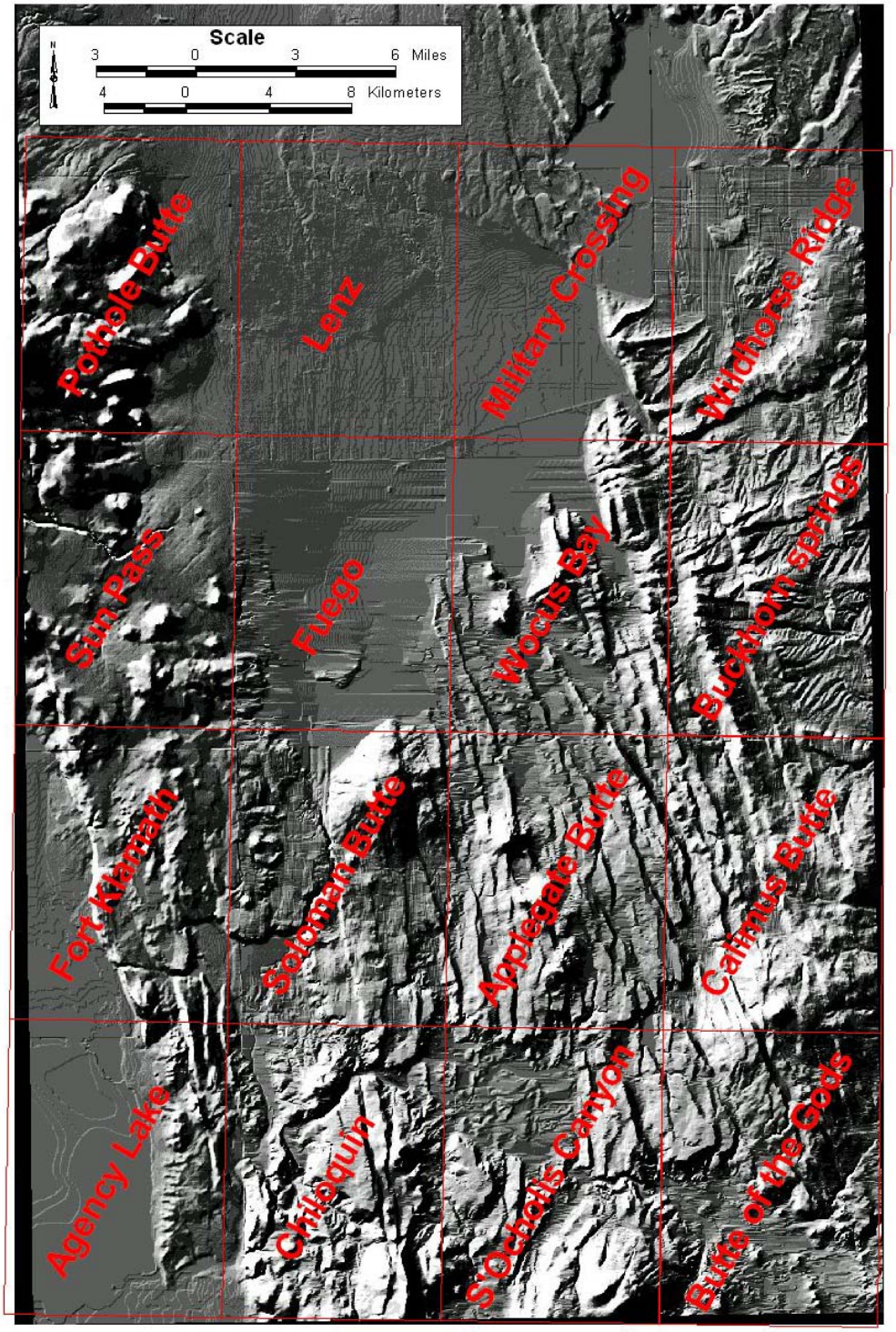

Figure 2: Vicinity of the study area in Klamath County, Oregon. The study area is comprised of the two U.S.G.S. 7.5 minute quadrangles in the center of the figure: Wocus Bay and Soloman Butte.

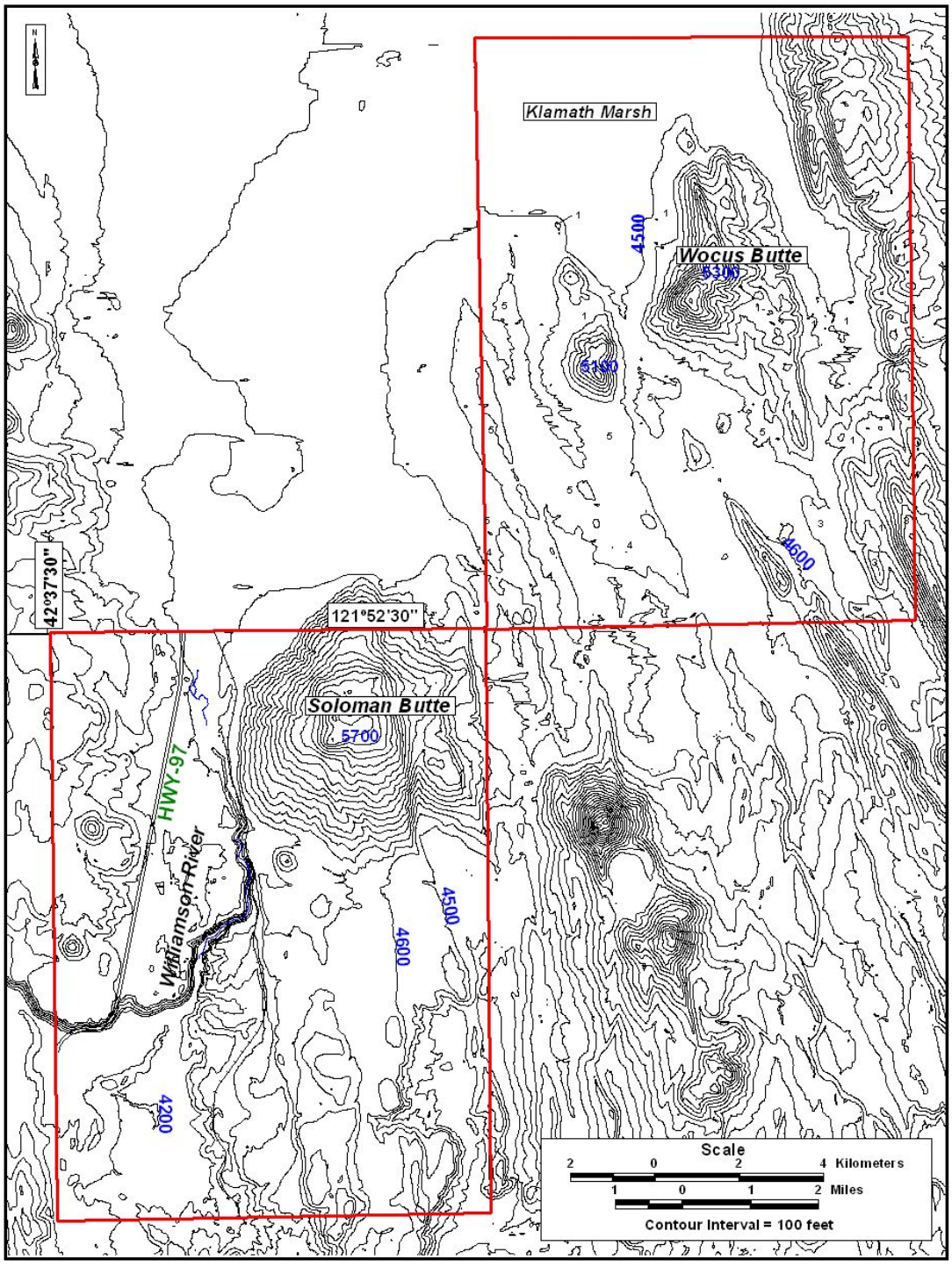

Figure 3: Topographic map of the study area in Klamath County, Oregon. The Soloman Butte quadrangle is in the lower left corner and the Wocus Bay quadrangle is in the upper right corner.

Volcanic Stratigraphy

The volcanic rocks of the study area have been divided into six sequences on the basis of lithology, geochemistry, and geochronology (Figure 4). Details on the lithology, stratigraphic relations and distribution are provided in Lee and Cummings (in review), and Conaway and Cummings (in press). The stratigraphic designations on these maps and the sequence assignment in the study area are presented in Table 1. The six sequences defined here consist only of effusive volcanic bedrock units; sedimentary, hydrovolcanic, and pyroclastic units described in the quadrangle map texts are not included.

Sequence 1 units are located in the Wocus Bay quadrangle in the northeastern part of the map area and extend into the neighboring quadrangles to the north (Military Crossing), east (Buckhorn Springs) and northeast (Wildhorse Ridge) (Figure 2, Appendix E). Sequence 1 samples are divided into interfingered alkali-rich and low-alkali suites; the geochemical distinction between these subdivisions is defined in the Petrology section. Alkali-rich lava flows range from basaltic trachyandesite to trachydacite/trachyte. Low-alkali lava flows range from basaltic andesite to andesite. Sequence 1 is late Pliocene and ranges in age from 3.68 (Wildhorse Ridge flow) to 4.09 Ma (Table 2).

Sequence 2 units compose late Pliocene low potassium, high-alumina olivine tholeiite (HAOT as defined by Hart et al., 1984) lava flows in the southern part of the map area extending south into the Chiloquin quadrangle (Figure 2, **Error! Reference**

source not found.). The western extent of these lava flows lies within the Soloman Butte quadrangle and,

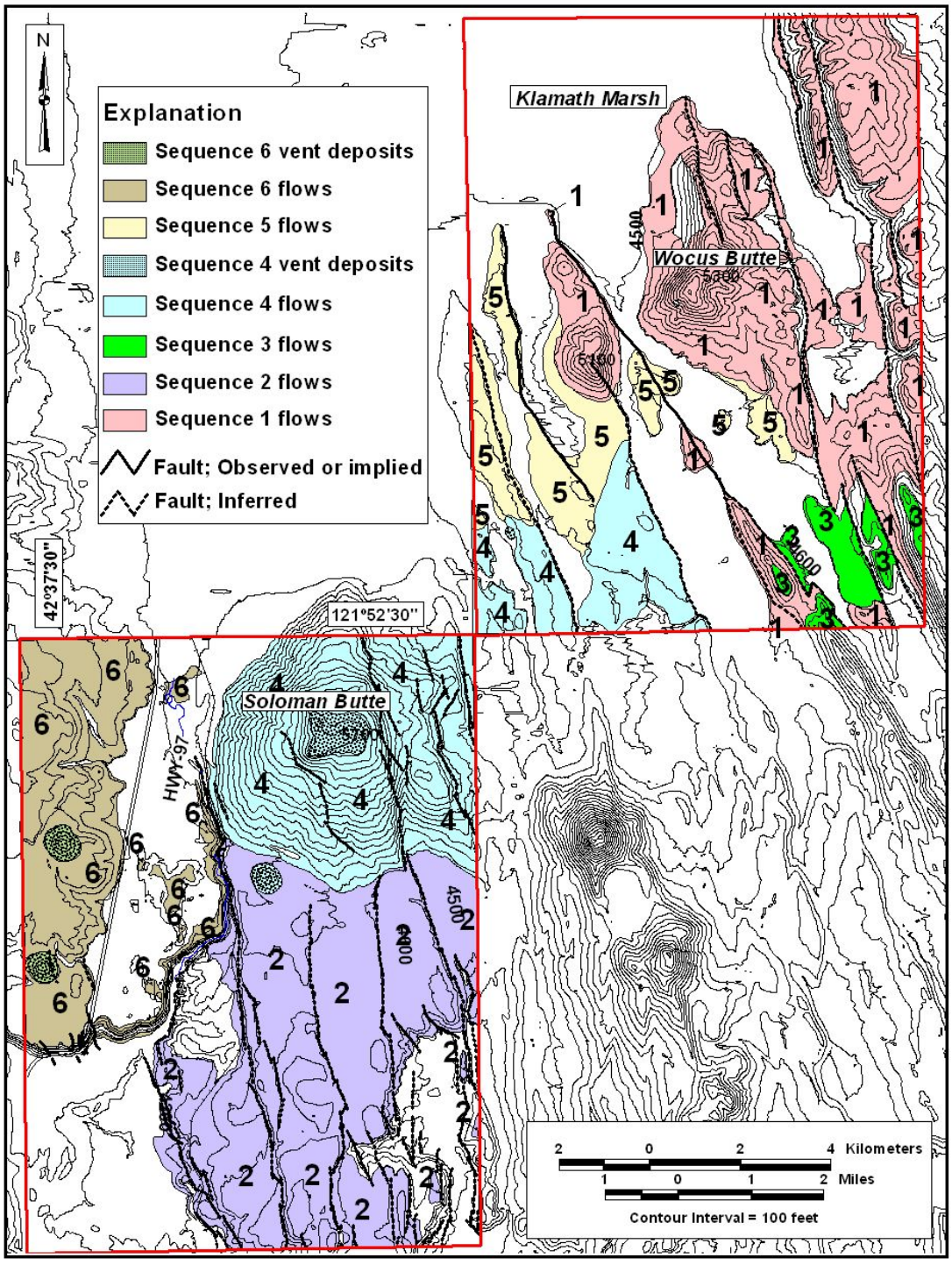

Figure 4: Geologic map of the study area in Klamath County, Oregon. Wocus Bay quadrangle in the upper right corner, Soloman Butte quadrangle in the lower left corner.

Table 1: List of volcanic bedrock sequences defined in this study and their corresponding map symbols on published 1:24000 scale geologic maps.

Map Unit (s)	Reference	Sequence (as defined in this study)
Qba, Qa, Qaks, Qbashv, Qbash, Qta, Tba	Lee and Cummings, in review	6
QTbkm	Conaway and Cummings, in press	5
QTasbv, QTasb	Lee and Cummings, in review	4
Tbhc	Conaway and Cummings, in press	4
Tbarb, Tbaf, Tbawh	Conaway and Cummings, in press	3
Tbf, Tbp	Lee and Cummings, in review	2
Tbawb, Ttlw, Tbam, Tbaw, Ta, Tbaw2, Tbyc	Conaway and Cummings, in press	1

to the north, they underlie sequence 4 rocks in the central part of the map area (Lee and Cummings, in review). The age of sequence 2 is constrained on the basis of stratigraphic relationships developed in Lee and Cummings (in review) and is believed to be approximately 3.0 Ma.

Sequence 3 units are composed of multiple late Pliocene basaltic andesite lava flows located along the central eastern map boundary. Sequence 3 overlies sequence 1 in the Wocus Bay quadrangle. These lava flows may extend into neighboring quadrangles to the south (Applegate Butte) and to the east (Buckhorn Springs) (Figure 2, **Error! Reference source not found.**). The age of sequence 3 is constrained on the basis of stratigraphic relationships developed in Conaway and Cummings (in press) and is

Table 2: Summary of whole rock $^{40}Ar/^{39}Ar$ age dates for selected samples in the Wocus Bay and Soloman Butte quadrangles, Klamath County, Oregon[1].

Sequence and Sample #	UTM Coordinates	Latitude Longitude	Age	Method	Reference
Sequence 1, Sample #3	610500 E 4741010 N	42º48'56.16" E 121º38'58.84" N	4.09 ± 0.05 Ma	$^{40}Ar/^{39}Ar$	Conaway and Cummings, in press
Sequence 1, Sample #4	609703 E 4741200 N	42º49'2.73" E 121º39'28.79" N	3.89 ± 0.08 Ma	$^{40}Ar/^{39}Ar$	Conaway and Cummings, in press
Sequence 1, Sample #113	611100 E 4743800 N	42º50'26.27" E 121º38'25.45"	4.08 ± 0.12 Ma	$^{40}Ar/^{39}Ar$	Conaway and Cummings, in press
Sequence 1, Sample #8	620806 E 4721471 N	42º38'17.30" E 121º31'35.18" W	3.68 ± 0.08 Ma	K-Ar	Sherrod and Pickthorn (1992)
Sequence 4, Sample #57	605790 E 4736900 N	42º36'45.34" E 121º42'23.97" N	2.05 ± 0.12 Ma	$^{40}Ar/^{39}Ar$	Conaway and Cummings, in press
Sequence 5, Sample #10	605772 E 4738234 N	42º47'28.59" E 121º42'23.86" N	1.62 ± 0.47 Ma	$^{40}Ar/^{39}Ar$	Conaway and Cummings, in press
Sequence 6, Sample #52	593621 E 4724774 N	42º40'17.99" E 121º51'26.61" N	1.14 ± 0.10 Ma	$^{40}Ar/^{39}Ar$	G. Preist, November 23, 1999, pers. comm.

[1]Analyses for sample #'s 3, 4, 10, 57, and 113 performed by P. W. Layer at the Geochronology Laboratory, University of Alaska (**Error! Reference source not found.**). Age date for sample #8 is age of Wildhorse Ridge flow in the mapping of Sherrod and Pickthorn (1992); Wildhorse Ridge flow is part of sequence 1 discussed here. Age date for sample #52 obtained from unpublished data of George Priest, Oregon Department of Geology and Mineral Industries. UTM coordinates are Zone 10, Datum NAD 83.

believed to be older than 2.05 ± 0.12 Ma (sequence 4 age) and younger than 3.0 Ma (sequence 2 age).

Sequence 4 units are composed of Plio-Pleistocene andesite and minor basaltic andesite lava flows with associated vent deposits located at Soloman Butte, a 300 m volcano in the central part of the map area. These lava flows and vent deposits are concentrated in the Soloman Butte quadrangle with earlier, underlying lava flows in the Wocus Bay quadrangle. These lava flows extend into neighboring quadrangles to the north (Fuego) and east (Applegate Butte) (Figure 2, **Error! Reference source not found.**). An $^{40}Ar/^{39}Ar$ age of 2.05 ± 0.12 Ma on one of the earliest lava flows from Soloman Butte suggests this volcanic center was active during late Pliocene and early Pleistocene time (Table 2).

Sequence 5 units are composed of Plio-Pleistocene basalt lava flows in the central portion of the study area just north of Soloman Butte (Figure 4). These lava flows extend into neighboring quadrangles to the west (Fuego) and to the north (Military Crossing) (Figure 2, **Error! Reference source not found.**). Vents for these lava flows may exist in the Wocus Bay quadrangle (Conaway and Cummings, in press). The age of sequence 5 is 1.62 ± 0.47 Ma (Table 2).

Sequence 6 units consist of multiple Pleistocene basaltic andesite, andesite and trachyandesite lava flows along the northwestern portion of the Soloman Butte quadrangle. These lava flows extend into neighboring quadrangles to the north (Fuego), to the northwest (Sun Pass), and to the east (Fort Klamath) (Wiley, in press) (Figure 2, **Error! Reference source not found.**). An $^{40}Ar/^{39}Ar$ age of 1.14 ± 0.10

Ma on one of the older basaltic andesite lava flows suggests sequence 6 units were emplaced during the middle Pleistocene.

Petrology

Petrography

The reader is referred to Table 3 for a concise summary of the distinguishing petrographic characteristics of the sequences, and to Appendix C for detailed petrographic descriptions and photomicrographs. The most petrographically distinct sequences are 1 and 2. Sequence 1 rocks generally have a trachytic texture, whether it forms patches, trachytic groundmass only, or as the dominant texture. Sequence 2 samples are nonporphyritic and diktytaxitic. Sequences 3, 4, and 6 have subtle differences in terms of modal mineralogy and textures, but are generally characterized by porphyritic texture with multiple populations of plagioclase phenocrysts. Sequence 5 is chiefly characterized by a phaneritic or porphyritic-aphanitic texture with sparse diktytaxitic cavities.

Geochemistry

Samples from each of the six volcanic bedrock sequences were geochemically analyzed. Sample locations are shown on Figure 5 and in tabular form in **Error! Reference source not found.**. The LeBas et al. (1986) IUGS geochemical classification of volcanic rocks based on total alkali and silica is used (Figure 6). This section also utilizes the volcanic rock classification scheme of Miyashiro (1975) which defines calc-alkalic and tholeiitic series lavas based on weight percent SiO_2 and FeO*/MgO (Figure 7). In addition, the

Table 3: Summary of petrographic characteristics of rocks in the Soloman Butte and Wocus Bay quadrangles, Klamath County, Oregon. Phenocryst phases are shown in bold-faced font. The following abbreviations are used: ol = olivine, opx = orthopyroxene, cpx = clinopyroxene, plag = plagioclase, FeTi = iron-titanium oxide, ap = apatite, hbl = hornblende.

Sequence Subdivision	**Texture(s)**	**% Phenocrysts**	**Mineralogy**
6 basaltic andesite	Porphyritic, rarely seriate	25-30%	**ol** + **opx** + **cpx** + **plag** + **FeTi** ± **ap**
6 andesite/ trachyandesite	Porphyritic, aphanitic, trachytic	3-8%	**plag** ± **ol** + **opx** + **cpx** + **FeTi** ± **ap** ± **hbl(?)**
5	Phaneritic or porphyritic-aphanitic with sparse diktytaxitic cavities	7-35%	**ol** + **plag** + **FeTi** ± **ap**
4	Porphyritic	30–35%	**ol** + **opx** + **cpx** + **plag** + **FeTi**
3	Trachytic	3 – 15 %	**ol** + **cpx** + **opx** + **plag** + **FeTi**
	Porphyritic with microporphyritic groundmass	40 – 50 %	**ol** ± **cpx** + **opx** + **plag** + **FeTi**
2	Diktytaxitic, subophytic to ophytic, nonporphyritic	< 1%	ol + opx + cpx + **plag** + FeTi
1 alkali-rich	Porphyritic with microporphyritic groundmass and diktytaxitic patches	< 5 %	**ol** + **plag** + **FeTi** ± **pyrox**
	Trachytic and aphanitic	Most << 1 % Rarely 1 – 4 %	**plag** + **FeTi** ± **cpx** ± **ol (?)**
	Porphyritic-aphanitic with glomerocrysts	4 – 14 %	**Plag** + **FeTi** ± **opx** ± **cpx** ± **ol** ± **hbl(?)**
1 low-alkali	Porphyritic-aphanitic	15 – 25 %	**ol** + **opx** ± **cpx** + **plag** + **FeTi**
	Porphyritic with microporphyritic groundmass	40 – 50 %	**ol** + **opx** + **plag** + **FeTi**
	Trachytic	< 2 %	**cpx** + **opx** + **plag** + FeTi

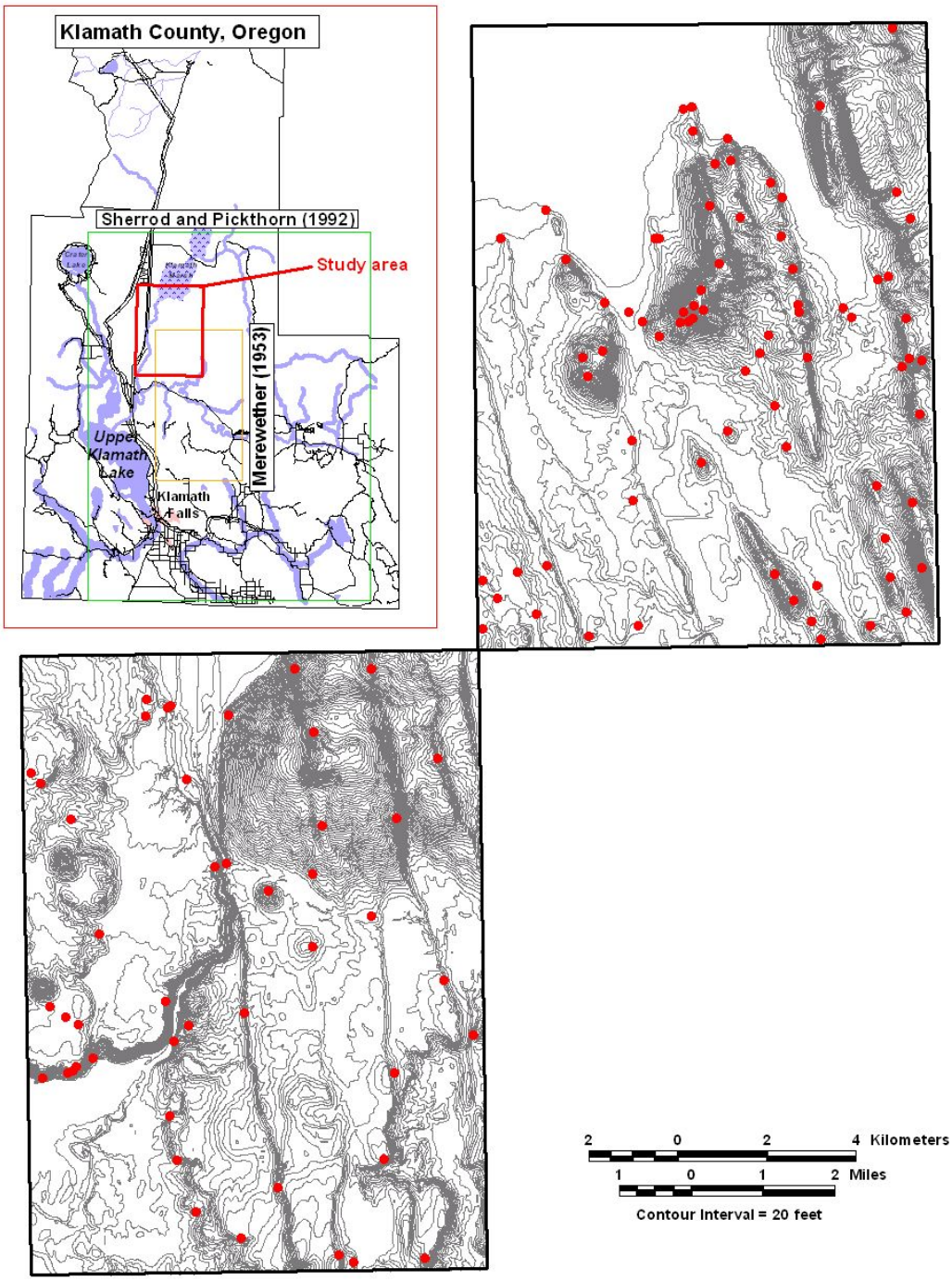

Figure 5: Geochemical and petrographic sample locations for the study area, Klamath County, Oregon. Upper right is Wocus Bay quadrangle and lower left is Soloman Butte quadrangle. Sample locations correspond to hand sample, thin section, XRF, and INAA samples gathered during 1998.

total alkali - total iron - magnesium diagram (AFM) of Irvine and Baragar (1971) is used to further define calc-alkalic and tholeiitic trends (Figure 8). Appendix F contains the average and standard deviation values of the concentrations of elements analyzed by XRF for the sequences. Element-element plots and C1 chondrite-normalized rare earth element (REE) plots are also used to characterize rock sequences.

Sequence 1

Classification

Sequence 1 rocks consist of late Pliocene basaltic andesite, basaltic trachyandesite, andesite, trachyandesite and trachydacite lava flows as shown on Figure 6. This sequence is subdivided into alkali-rich and low-alkali subdivisions on the basis of K_2O and Na_2O concentrations (Figure 9). The alkali-rich subdivision has consistently higher K_2O and significantly higher Na_2O concentrations than the low-alkali subdivision. Basaltic andesite and andesite lava flows comprise the low-alkali subdivision and basaltic trachyandesite, trachyandesite and trachydacite lava flows make up the alkali-rich subdivision. Low-alkali samples plot near FeO*/MgO = 1.5-2.5 and cross the line that separates calc-alkalic and tholeiitic suites on a FeO*/MgO versus SiO_2 diagram (Figure 7). When plotted on an AFM diagram, the low-alkali subdivision samples follow a calc-alkalic trend and the alkali-rich samples plot in the tholeiitic field very near the line that separates calc-alkalic and tholeiitic suites (Figure 8).

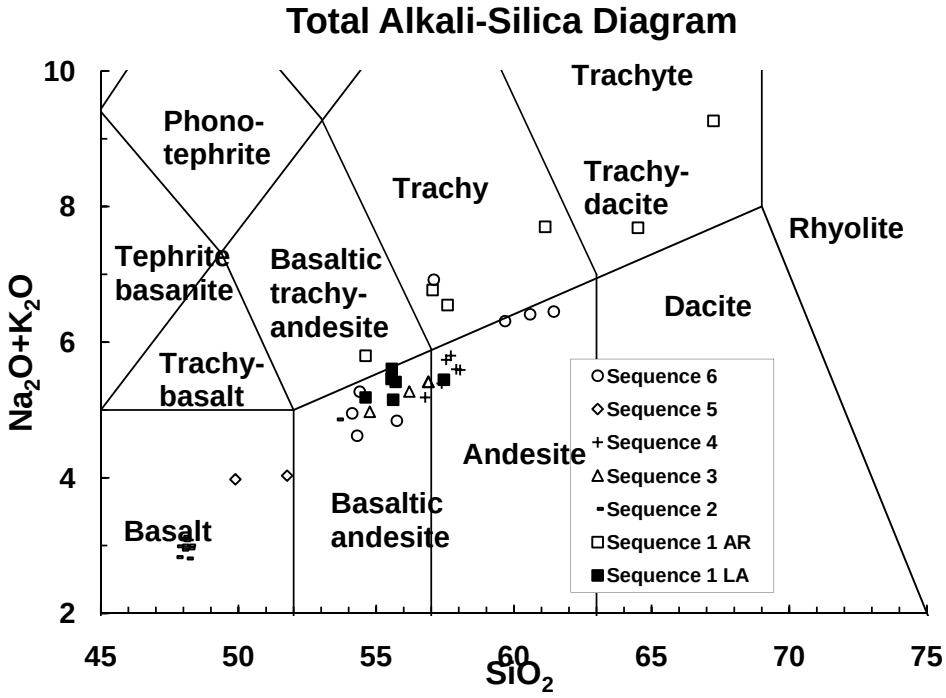

Figure 6: Total alkali-silica diagram after LeBas et al. (1986). In this diagram, 45 – 52 % SiO2 = basalt, ≥ 52 – 57 % SiO2 = basaltic andesite, ≥ 57 – 63 % SiO2 = andesite, and ≥ 63 – 77 % SiO2 = dacite. AR = alkali-rich and LA = low-alkali. Analyses by XRF.

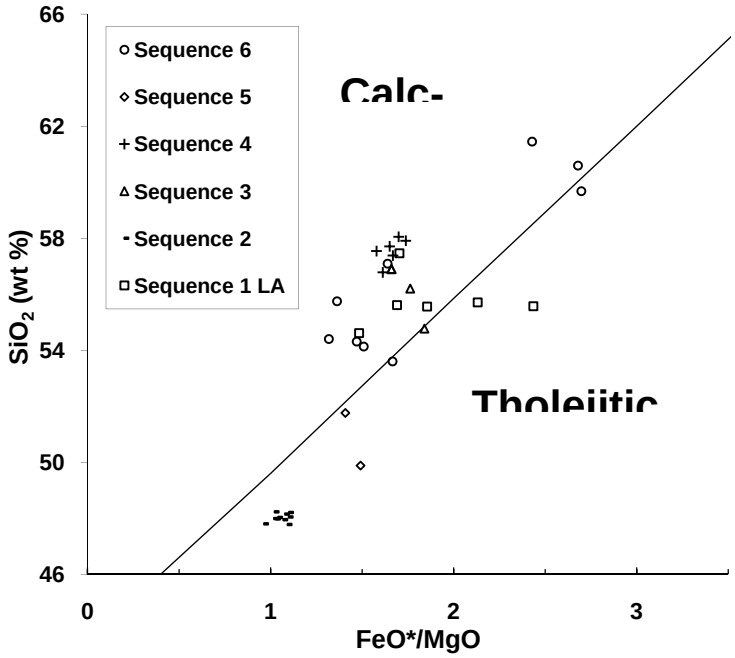

Figure 7: Determination of calc-alkalic versus tholeiitic suites after Miyashiro (1975). Analyses by XRF.

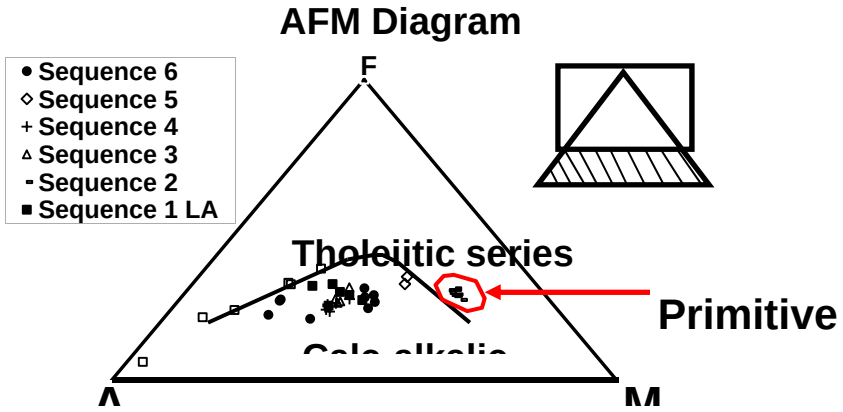

Figure 8: Total alkali-total iron-magnesium diagram after Irvine and Baragar (1971). Solid line separates calc-alkaline and tholeiitic suites. A = Na_2O+K_2O, F = FeO*, M = MgO. Analyses by XRF.

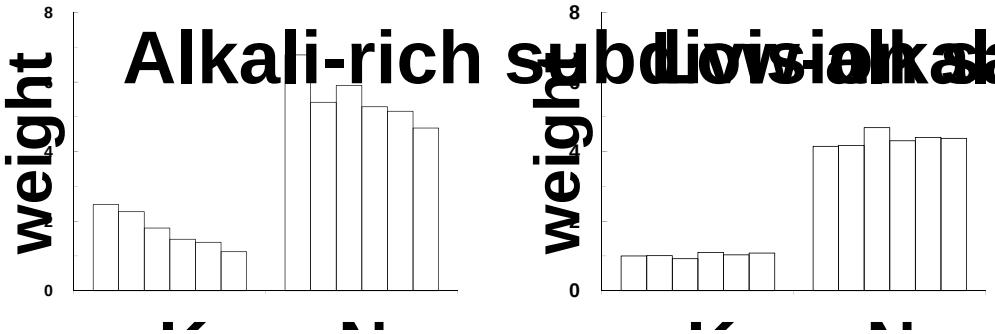

Figure 9: Alkali content of sequence 1 samples. Columns represent the concentrations of K_2O and Na_2O for each sample in each subdivision. The alkali-rich samples consist of basaltic trachyandesite, trachyandesite, and trachydacite. The low-alkali samples consist of basaltic andesite.

Low-alkali subdivision geochemical characteristics

The low-alkali subdivision is interlayered with the alkali-rich subdivision and is distinguished from the alkali-rich subdivision by its lower alkali content (Figure 9) and incompatible elements, and higher concentrations of compatible elements. Like the alkali-rich subdivision, the low-alkali subdivision is also characterized by wide ranges of concentrations of major, minor and trace elements when compared to other sequences in the map area (Appendix G). These samples are more compatible element enriched and incompatible element depleted than the alkali-rich subdivision (Appendix G). On Figure 10, the low-alkali REE pattern is characterized by lower concentrations of REE than the alkali-rich subdivision, LREE enrichmment, and divergent Eu behavior (i.e., some samples show positive Eu anomalies while others show negative Eu anomalies).

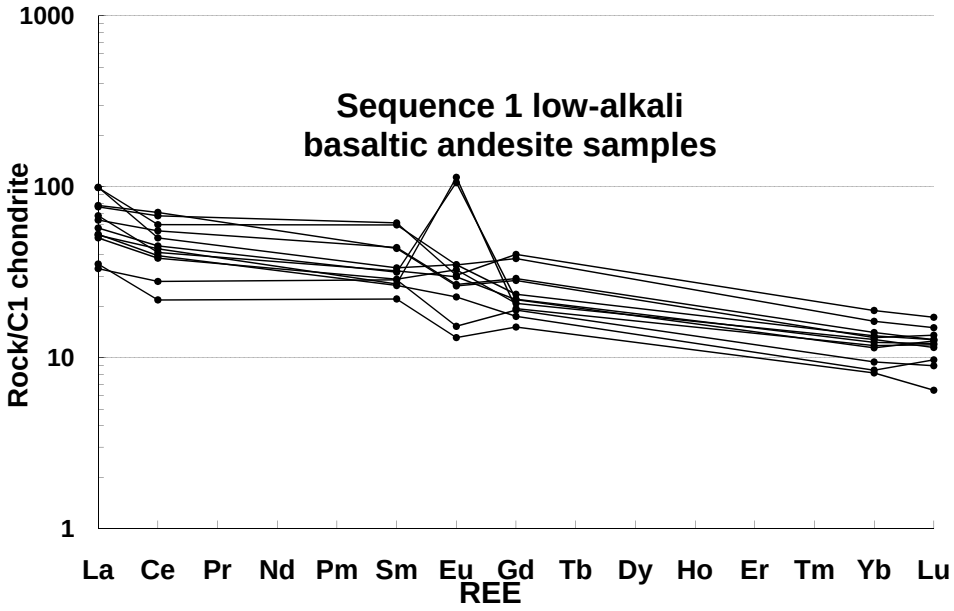

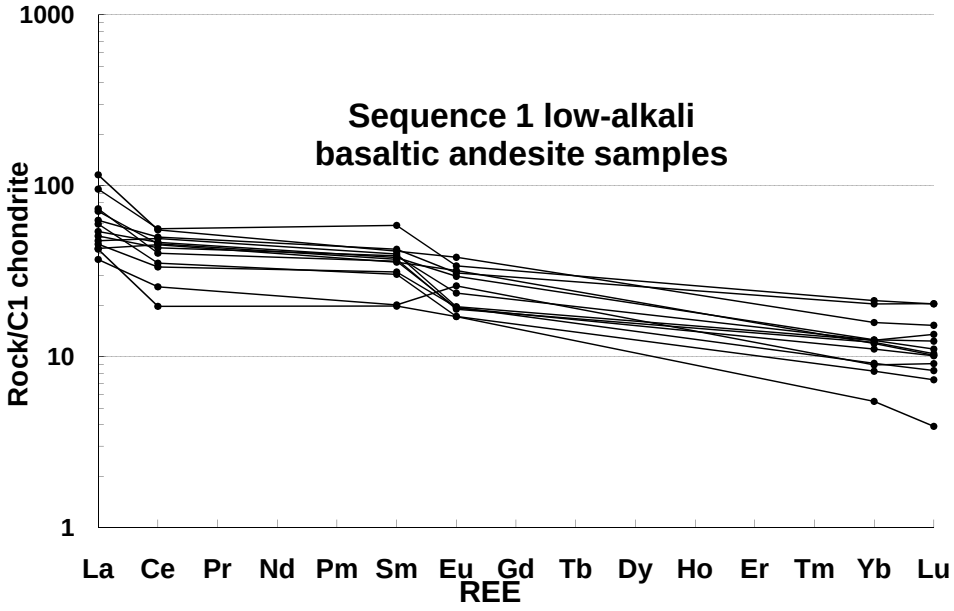

Figure 10: C1 chondrite-normalized rare earth element (REE) diagram for all low-alkali basaltic andesite samples of sequence 1. Gd interpolated between Sm and Yb values for upper graph. For lower graph, trend interpolated between data points for Pr, Nd, Pm, Gd, Tb, Dy, Ho, Er, and Tm. Analyses by INAA.

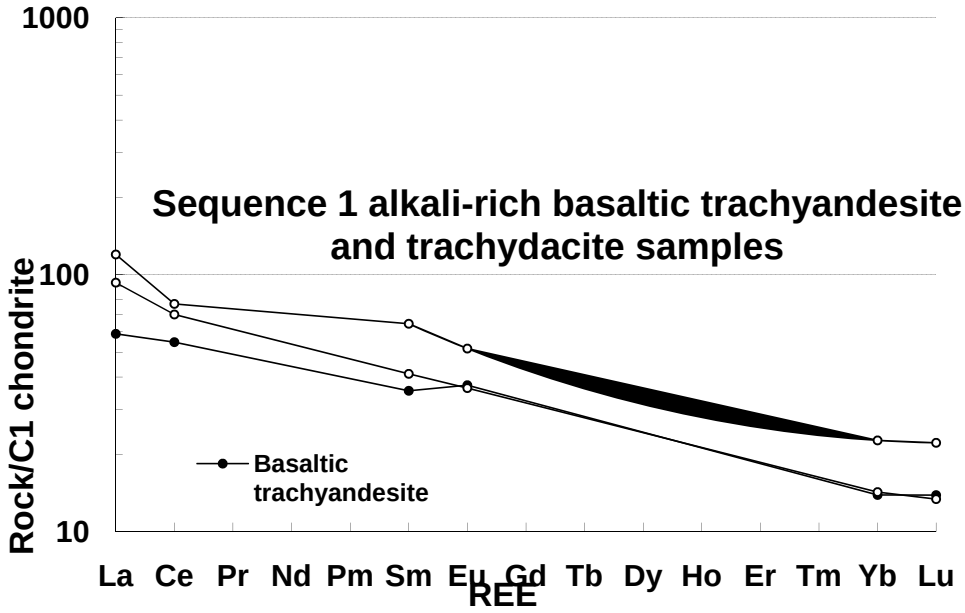

Figure 11: C1 chondrite-normalized rare earth element (REE) diagram for alkali-rich basaltic trachyandesite and trachydacite samples of sequence 1.Trend interpolated between data points for Pr, Nd, Pm, Gd, Tb, Dy, Ho, Er, and Tm. Analyses by INAA.

Alkali-rich subdivision geochemical characteristics

Sequence 1, alkali-rich subdivision samples are characterized by a diverse suite of rocks that contain between 54.61 and 67.25 weight percent SiO_2. This subdivision comprises the most evolved suite of rocks within the map area (with respect to wt % SiO_2), and the lowest concentrations of Al_2O_3 (16.55 to 17.36 wt %). These samples also have wide ranges of major element oxides and the highest alkali (particularly Na_2O) concentrations of rocks from all the sequences. This subdivision also has the highest and most variable concentrations of incompatible trace elements and the lowest concentrations of compatible trace elements (of all sequences) (Figure 15 and Appendix G). Figures 11 and 12 show the C1 chondrite-normalized REE patterns for alkali-rich samples of sequence 1. The REE pattern is characterized by a light REE

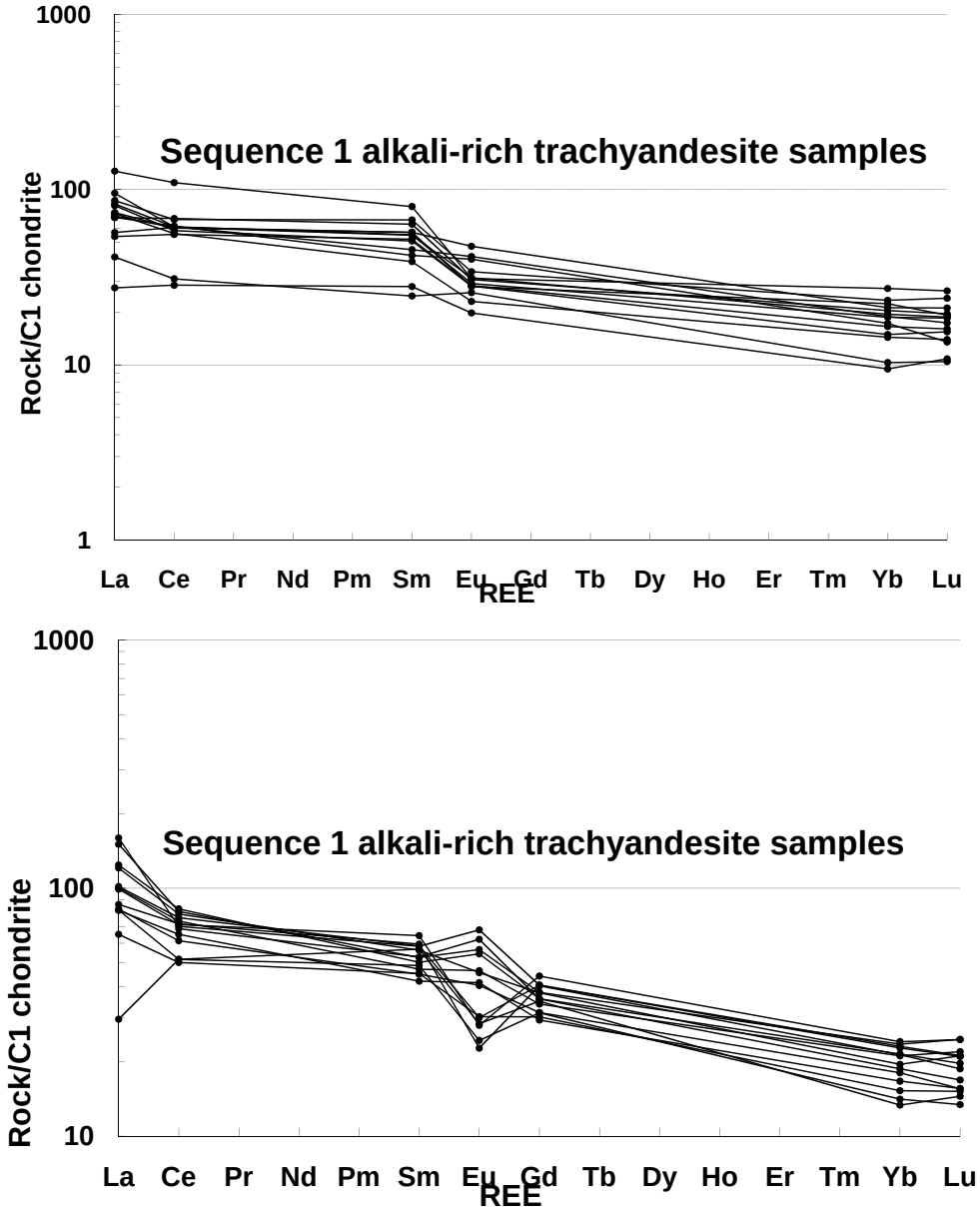

Figure 12: C1 chondrite-normalized rare earth element (REE) diagram for alkali-rich trachyandesite samples of sequence 1. Gd interpolated between values for Sm and Yb for lower graph. For upper graph, trend interpolated between data points for Pr, Nd, Pm, Gd, Tb, Dy, Ho, Er, and Tm. Analyses by INAA.

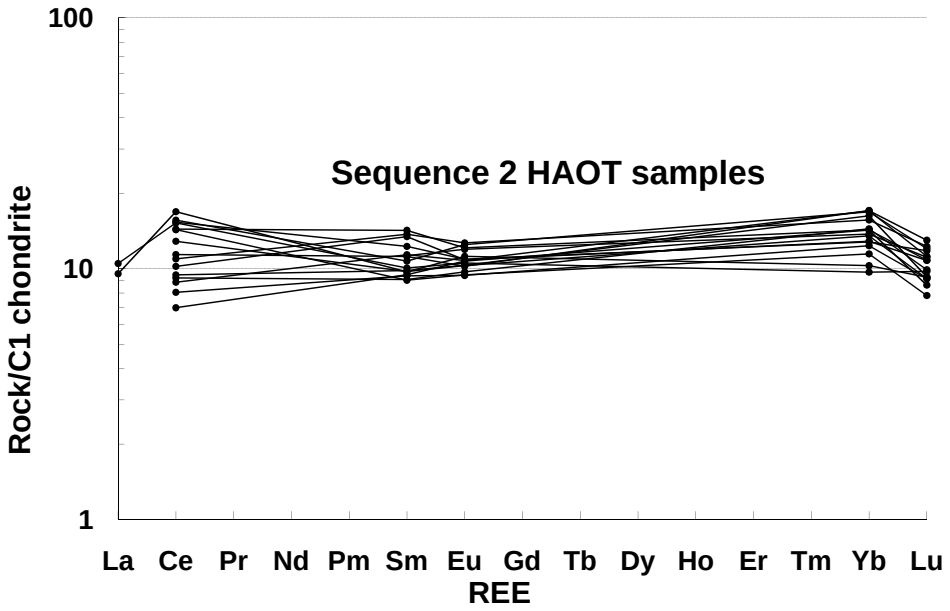

Figure 13: C1 chondrite-normalized REE diagram for sequence 2 HAOT. Trend interpolated for Pr, Nd, Pm, Gd, Tb, Dy, Ho, Er, and Tm. Analyses by INAA.

(LREE) enrichment pattern, high concentrations of REE (over 100x chondrite), and negative Eu anomalies, although a few samples exhibit positive Eu anomalies.

Sequence 2

Classification

Sequence 2 rocks are low-K, high-alumina olivine tholeiite (low-K ≤ 0.39 wt %, high-alumina > 16 wt % HAOT as defined by Hart et al., 1984). These rocks lie within the center of the basalt field on Figure 6. Sequence 2 is also classified as tholeiitic series lavas using the classification schemes of Miyashiro (1975) and Irvine and Baragar (1971) (Figures 7 and 8). In addition, sequence 2 rocks plot within the area defined as primitive HAOT on Figure 8.

Geochemical characteristics

The late Pliocene HAOT samples of sequence 2 comprise the least modified lavas in the map area. The samples usually plot as a tight, easily distinguishable cluster on standard classification diagrams and element-element plots. These samples have the characteristic incompatible element depletion and compatible element enrichment patterns of primitive lavas (Figure 15, Appendix G), display relatively flat REE patterns with slight heavy REE (HREE) enrichment, and the lowest REE concentrations of all sequences (near 10x chondrite) (Figure 13).

Sequence 3

Classification

Sequence 3 rocks are classified as basaltic andesite (Figure 6). When classified using the diagram of Miyashiro (1975), the samples are calc-alkalic series lavas with one sample that plots on the line that separates calc-alkalic and tholeiitic suites (Figure 7). When plotted on the AFM diagram of Irvine and Baragar (1971), sequence 3 samples plot within the calc-alkalic field (Figure 8).

Geochemical characteristics

Sequence 3 samples are characterized by their divergent behavior in terms of trace elements when compared to basaltic andesites of sequences 1, 4, and 6. While the four sequences (sequence 1, low-alkali subdivision, sequence 3, sequence 4, and sequence 6) plot together in terms of major oxides, trace elements such as Ba, Rb, Ni, Cr, Cu, Zr, V, Nb act as discriminators (Figure 15, Appendix G). Sequence 3 has lower concentrations of large ion lithophile (LIL) elements (Ba, Rb) and transition elements (Ni, Cr, Cu, and V), and higher concentrations of high field strength

elements (HFSE) (Zr and Nb). Sequence 3 samples also display moderate to strong LREE enrichment patterns, the highest concentrations of REE (except La of sequence 4) among the basaltic andesite samples of sequences 1, 3, 4, and 6, and positive Eu anomalies (Figure 14).

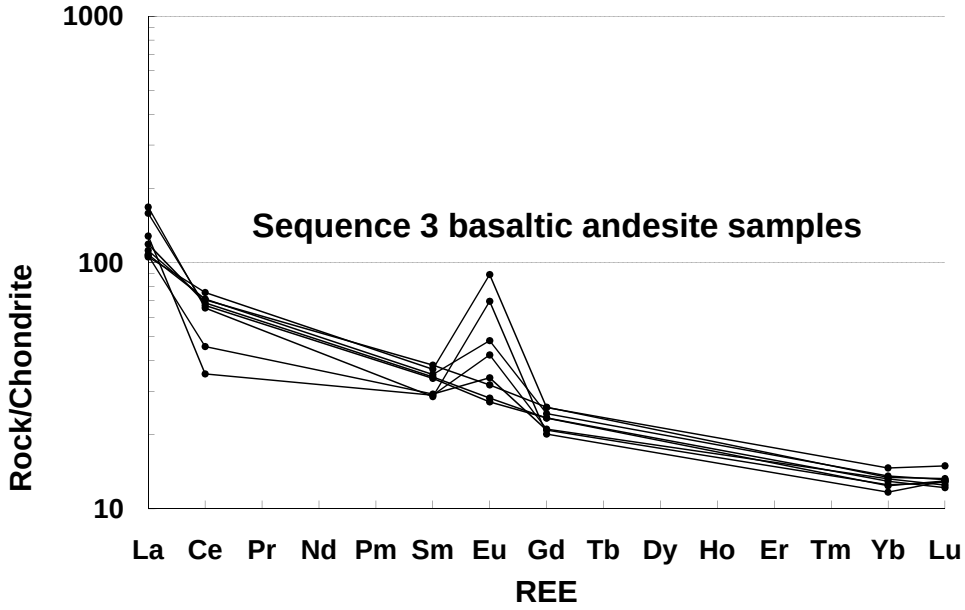

Figure 14: C1 chondrite-normalized REE diagram for sequence 3. Gd interpolated between values for Sm and Yb. Trend interpolated between data points for Pr, Nd, Pm, Tb, Dy, Ho, Er, and Tm. Analyses by INAA.

Sequence 4

Classification

Sequence 4 rocks consist of earlier basaltic andesite lava flows that progressively grade with time to andesite lava flows and culminate in andesitic vent deposits (Figure 6). When classified using the scheme of Miyashiro (1975), sequence 4 rocks plot as a tight cluster in the calc-alkalic field (Figure 7). These samples also

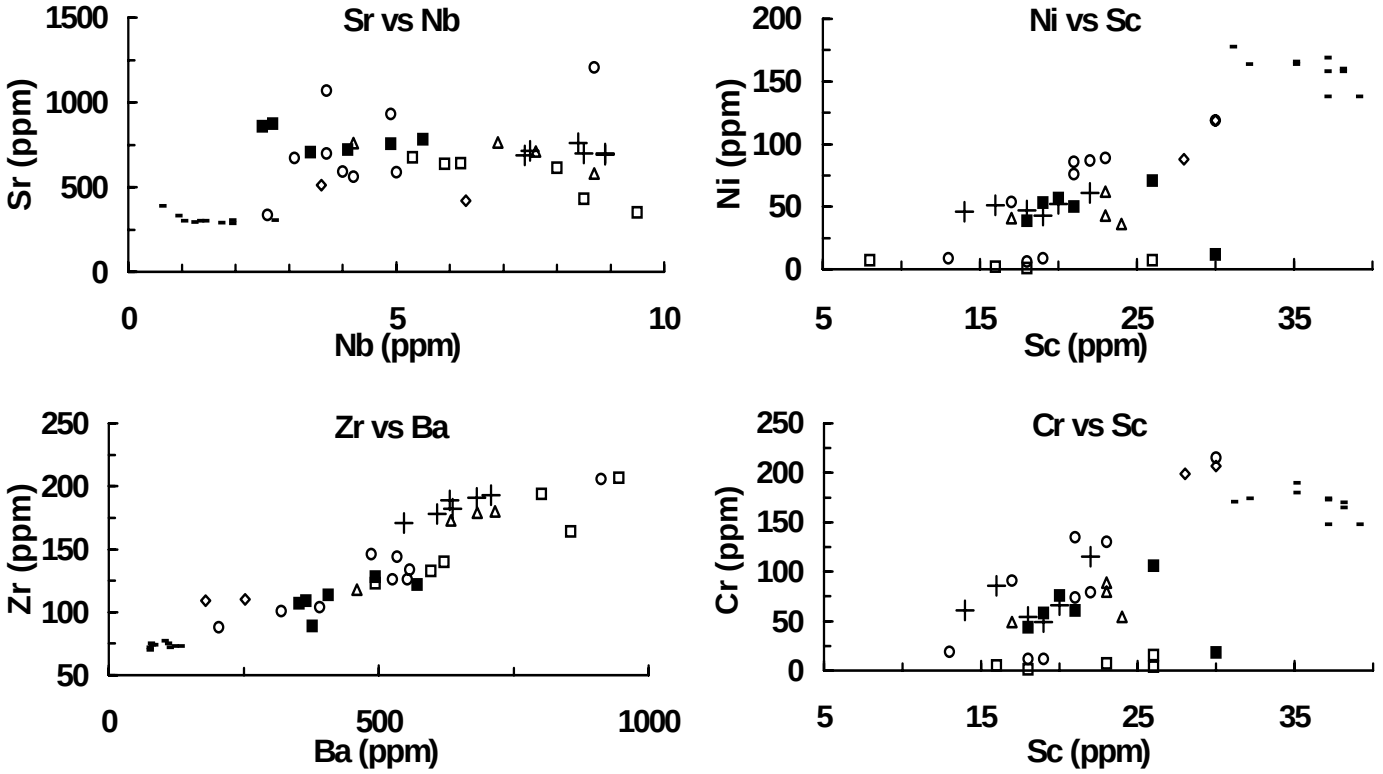

Figure 15: Standard element-element plots. Open squares are alkali-rich sequence 1, filled squares are low-alkali sequence 1 samples. Dashes are sequence 2, triangles are sequence 3, plus signs are sequence 4, diamonds are sequence 5, and open circles are sequence 6. Analyses by XRF.

plot as a tight cluster in the calc-alkalic field on the AFM diagram of Irvine and Baragar (1971) (Figure 8).

Geochemical characteristics

Sequence 4 samples are characterized by narrow ranges of all elements causing sequence 4 samples to plot as a cluster on various element-element plots and classification diagrams (Figures 6, 7, 8, 15). Sequence 4 samples tend to plot with sequence 3 basaltic andesites on these diagrams. Sequence 4 shows more compatible element enrichment and incompatible element depletion than andesites of sequence 6. Sequence 4 basaltic andesite and andesite samples display strong LREE enrichment patterns, and the andesite samples have overall REE concentrations less than those of the basaltic andesites of sequence 4. In addition, the andesites display only very slight negative and positive Eu anomalies, while the basaltic andesites show much more pronounced negative and positive Eu anomalies (Figure 16). The andesitic vent deposit has a very slight positive europium anomaly, lower REE concentrations (near 30x chondrite), and slight to moderate LREE enrichment.

Sequence 5

Classification

Sequence 5 rocks are high-alumina (> 16 wt %) olivine basalts (HAB). These rocks are not low-potassium HAOT as defined by Hart et al. (1984); this sequence has > 0.39 weight percent K_2O and > 1.35 weight percent TiO_2. These samples most closely resemble the low-potassium (K_2O < 0.5 wt %), low-Ti (TiO_2 < 2.0 wt %) transitional tholeiites (LKLT) discussed in Hart et al. (1984), but one sample has K_2O > 0.50 wt %. These HAB's plot within the basalt field in Figure 6. Sequence 5 rocks

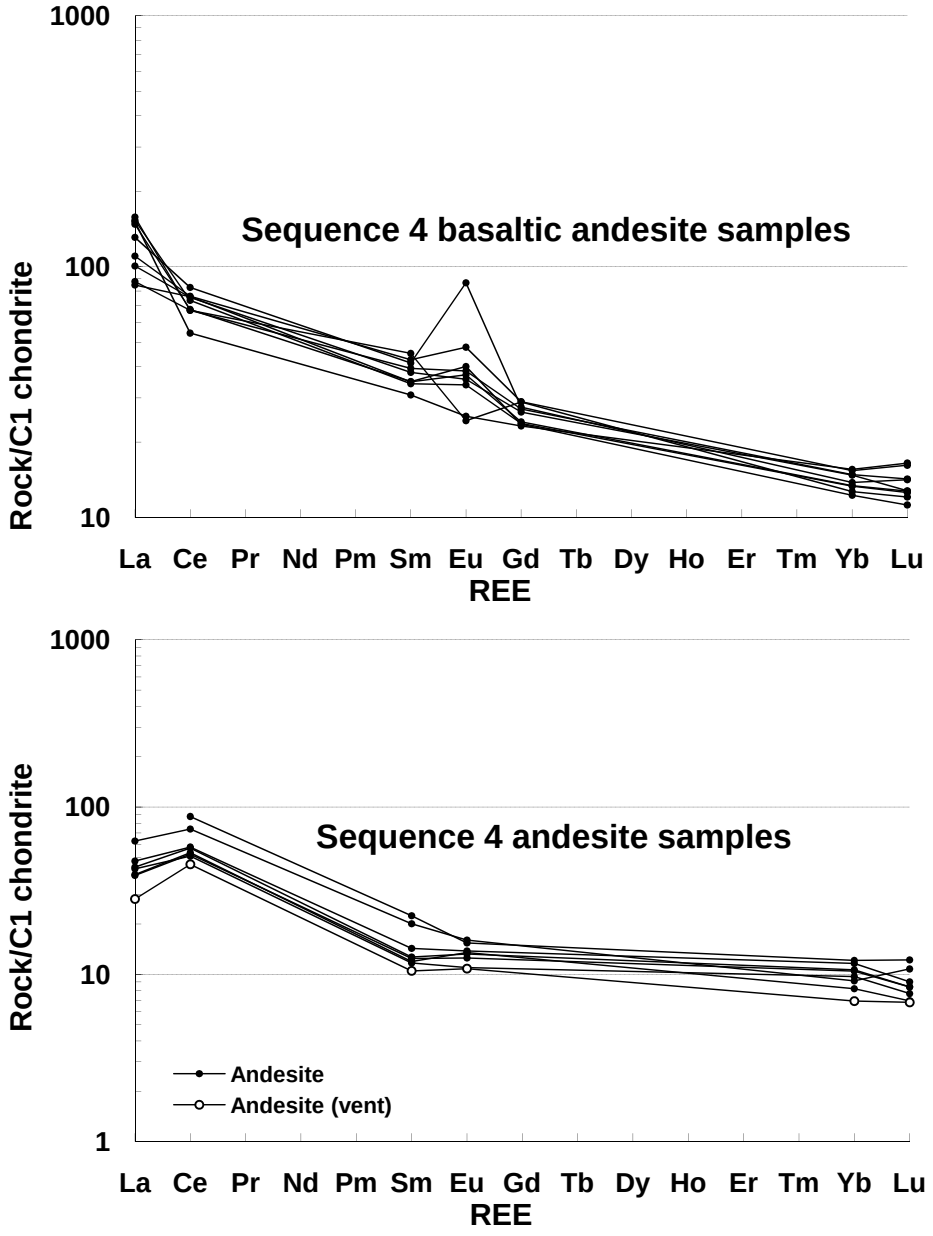

Figure 16: C1 chondrite-normalized REE diagram for sequence 4. Gd interpolated between values for Sm and Yb for upper graph. For lower graph, trend interpolated between data points for Pr, Nd, Pm, Gd, Tb, Dy, Ho, Er, and Tm. Analyses by INAA.

lie within the tholeiitic field on Figure 7, but lie within the calc-alkalic field on Figure 8. This discrepancy is due to the influence of the alkali content. The HAB's are tholeiitic series lavas with a high alkali content.

Geochemical characteristics

Sequence 5 rocks are characterized by their higher concentrations of incompatible elements and lower concentrations of compatible elements and mafic oxides relative to the HAOT's of sequence 2. Sequence 5 HAB's display slight LREE enrichment patterns near 50x chondrite (Figure 17). Three out the four samples do not display a Eu anomaly, while the remaining sample displays a strong positive Eu anomaly.

Sequence 6

Classification

Sequence 6 rocks consist of multiple interlayered lava flows of basaltic andesite, andesite and trachyandesite (Figure 6). These lava flows are calc-alkalic series lavas, although two samples fall very near the line that separates calc-alkalic and tholeiitic suites on Figure 7. When plotted on an AFM diagram, all lava flows lie within the calc-alkalic field (Figure 8).

Geochemical Characteristics

Sequence 6 rocks have the highest Al_2O_3 (17.12 to 19.35 wt %) and Sr (336 to 1207 ppm) of all the rock sequences. Many major and trace element concentrations are in the range of sequence 1 alkali-rich concentrations (e.g., Al_2O_3, Na_2O, P_2O_5, Ba Rb, Sr, and Zr). Sequence 6 samples usually plot as two distinct clusters (one basaltic andesite, one andesite/trachyandesite) on element-element plots (Figure 15). This

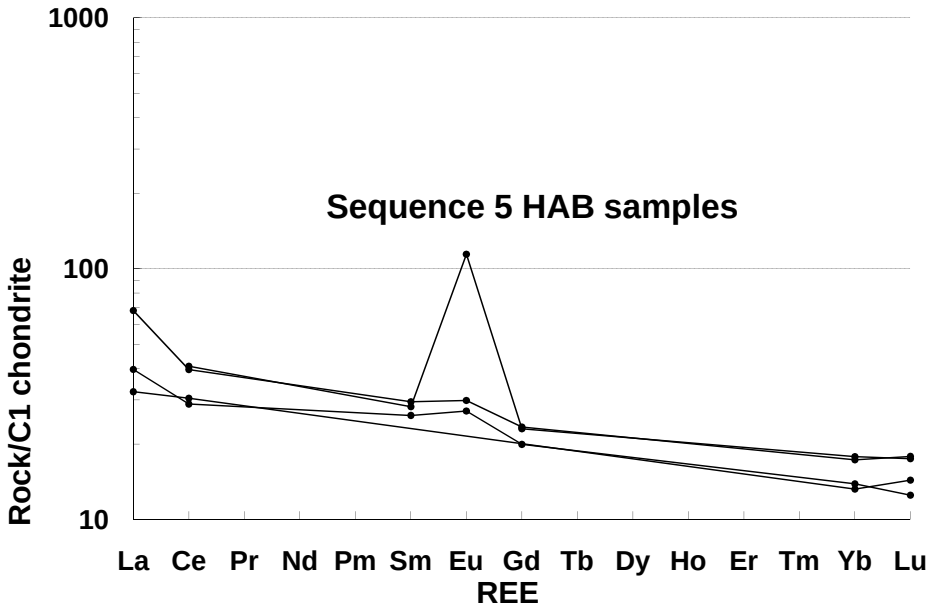

Figure 17: C1 chondrite-normalized REE diagram for sequence 5. Gd interpolated between values for Sm and Yb. Trend interpolated between data points for Pr, Nd, Tb, Pm, Dy, Ho, Er, and Tm. Analyses by INAA.

sequence is characterized by wide ranges of concentrations of major, minor and trace elements (Appendix G). Sequence 6 lava flows show incompatible element enrichment and compatible element depletion trends on element-element plots (Figure 15). Sequence 6 basaltic andesite REE patterns are characterized by slight LREE enrichment, relatively low concentrations near 40x chondrite, and a few samples show very slight positive Eu anomalies (Figure 18). Andesite and trachyandesite samples show more LREE enrichment than the basaltic andesite samples, and have slightly higher concentrations (near 50x chondrite). Four out of five of the trachyandesite samples display slight positive Eu anomalies, while the remaining sample along with the andesite samples do not display Eu anomalies.

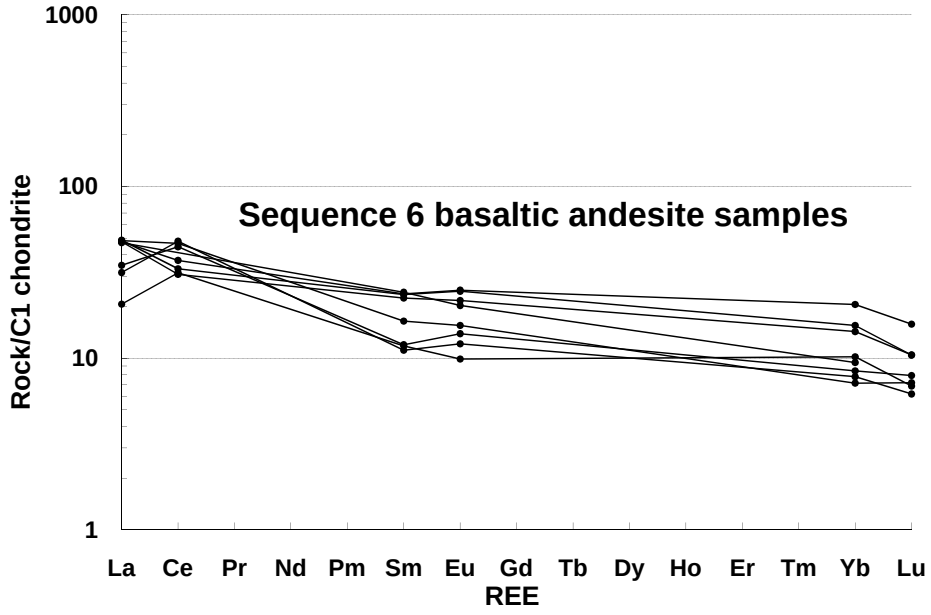

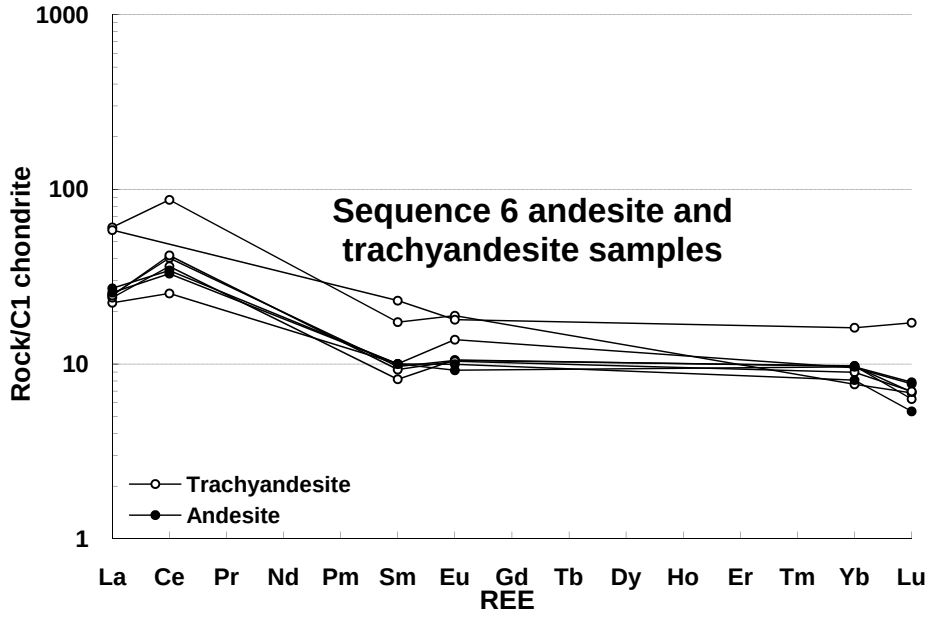

Figure 18: C1 chondrite-normalized REE diagrams for sequence 6. Trend interpolated for Pr, Nd, Pm, Gd, Tb, Dy, Ho, Er, and Tm. Analyses by INAA.

Summary of geochemistry

Rocks in the study area consist of primitive basalt to alkali-rich compositions that have been divided into six sequences. Each sequence can be recognized on various geochemical classification diagrams, element-element plots and REE diagrams. The following paragraphs highlights the basic geochemical patterns observed for each sequence.

Sequence 1 is characterized by its variability; the wide ranges of all major, minor and trace element concentrations are displayed in the scatter of points on geochemical variation diagrams. The trachytic alkali-rich samples of sequence 1 display systematic decrease in mafic oxides and compatible elements (TiO_2, FeO*, CaO, MgO, Sc, Cu) and increase in incompatible elements (K_2O, Na_2O, Ba, Rb, Zr, Nb, Pb, La) with increasing silica content (exception: Sr decreases with increasing silica). P_2O_5 has an initial increase followed by a steady decrease with increasing silica. These patterns are maintained on Figure 15, which contains plots of incompatible versus compatible elements. The observed pattern is consistent with a liquid line of descent beginning with the composition of sample #118 (basaltic trachyandesite, Appendices C, G, and H) and is examined in more detail in the geochemical modeling section. In addition, other magmatic processes (e.g., contamination, magma mixing) are explored; a combination of processes may be responsible for the geochemical behavior of the alkali-rich samples.

Low-alkali subdivision samples of sequence 1 display variable REE patterns and, like the alkali-rich subdivision, are also characterized by wide ranges of element

concentrations. The low-alkali subdivision is distinguished from the alkali-rich subdivision by more compatible element enrichment and lower concentrations of incompatible elements. The low-alkali subdivision is generally distinguished from sequence 3 basaltic andesites by its lower high field strength element (HFSE) concentrations, and from sequence 6 basaltic andesites by lower concentrations of compatible elements and higher concentrations of incompatible elements. The *Discussion* section provides a brief outline of the possible magmatic processes acting to produce andesite lavas in the study area.

Sequence 2 consists of primitive HAOT samples that plot as a tight cluster of points on all types of geochemical plots. This sequence seems to be geochemically unrelated to any other sequence in the map area. Sequence 2 HAOT display a relatively unmodified geochemical signature; the HAOT have similar compositions to mid-ocean ridge basalts (Hart et al., 1984). The primitive character of sequence 2 HAOT is evaluated in the geochemical modeling section.

Sequence 3 rocks are characterized by higher HFSE concentrations, lower LIL and transitional element concentrations, and a stronger LREE enrichment pattern compared to basaltic andesites of sequences 1 and 6. While these rocks are not modeled here, a discussion of andesite production in the study area is explored in the *Discussion* section.

Sequence 4 rocks are recognized on most geochemical plots as a tight cluster. Sequence 4 is geochemically unique in that these samples have the highest REE concentrations and strongest LREE enrichment pattern of all sequences. This

sequence is also characterized by variable LIL and transition element concentrations, and HFSE concentrations consistent with basaltic andesite/andesite compositions. Minor and trace element patterns indicate that these lava flows may follow a calc-alkaline fractionation trend beginning with the composition of sample #118 (Appendices A, B and G). With respect to the oxides, a normal compositional fractionation trend is followed where the vent deposit has the lowest concentrations of mafic oxides. In addition, this trend is continued with compatible elements (Ni, Cr, Sc, Zn). By contrast, the incompatible elements, Ba, Rb, Sr, Zr, Nb, and REE decrease with increasing silica content.

Sequence 5 is characterized by its HAB composition. These samples plot as a cluster on all geochemical diagrams. Sequence 5 HAB's are distinguished from sequence 2 HAOT's by their higher concentrations of incompatible elements and lower concentrations of compatible elements. Sequence 5 rocks may follow a fractionation trend as incompatible elements (K_2O, Na_2O, P_2O_5, Ba, Rb, Zn, Zr, Th, V, Y, Nb) increase while compatible elements (mafic oxides, Ni, Cr, Sc) decrease with increasing silica, although these trends are difficult to discern due to a low number of sample points. The incompatible element enrichment and compatible element depletion patterns are shown on element-element plots on Figure 15 and Appendix G.

Finally, sequence 6 rocks plot as two clusters on geochemical plots and are characterized by their variability. Although not as variable as sequence 1 rocks, these samples have wide ranges of major, minor, and trace elements (Appendix G).

Sequence 6 andesite samples also display a flatter REE pattern (less LREE enrichment) when compared to other andesites and more evolved rocks. In addition, the andesite and trachyandesite samples display lower REE concentrations than the basaltic andesite samples (which is unexpected), but do show stronger LREE enrichment (which is expected). Given the geochemical variability of these samples, it is difficult to discern which magmatic processes these lavas have experienced, although observed petrographic characteristics are consistent with magma mixing. A brief discussion of the production of andesites in the study area is provided in the *Discussion* section.

Geochemical Modeling

The following section presents geochemical models of the alkali-rich subdivision of sequence 1 and sequence 2 HAOT samples. Because sequence 1 rocks exhibit incompatible element enrichment and compatible element depletion trends with respect to increasing silica content (Figure 15 and Appendix G), the liquid line of descent of this sequence is modeled here in order to evaluate the pressure, temperature, oxygen fugacity, and water content of the parental magma. The parental composition is assumed to be similar to the least evolved sample compositions within the sequence. Sequence 2 basalts are also modeled here in order to evaluate their similarities and differences to primary (unmodified) mantle melts, and other HAOT in the vicinity of the study area.

The remaining sequences (1 [low-alkali subdivision], 3, 4, 5, and 6) are not modeled. Sequences 1 [low-alkali], 3, 4, and 6 rocks are of intermediate composition (chiefly basaltic andesite and andesite) and represent a complex magmatic history. In order to characterize the magmatic processes acting to produce these andesites, a larger region of study and a greater number of samples are required. For these reasons, the andesites of sequences 1, 3, 4, and 6 are not modeled; however, a brief discussion and the possible magmatic processes that produced them are detailed in the next section. Sequence 5 basalts are not modeled simply because there are too few geochemical analyses available.

The following section uses the Rayleigh crystal fractionation equation $C_L/C_O = F^{(D-1)}$ where C is the concentration of the element in the parent magma (C_O) and in the daughter magma (C_L), F is the percent remaining liquid, and D is the partition coefficient. This equation is used to model the crystal fractionation paths of trace elements of sequence 1, alkali-rich subdivision. Liquid lines of descent of major oxides are modeled by the computer modeling program COMAGMAT (Ariskin, 1992).

Sequence 1 alkali-rich subdivision

The alkali-rich subdivision of sequence 1 is modeled here in terms of crystal fractionation paths because the samples show incompatible element enrichment and compatible element depletion trends on key element-element plots (Appendices G and H). These successive incompatible element enrichment and compatible element depletion trends with respect to increasing silica content can be indicative of crystal

fractionation of a parental magma. Sample # 118, basaltic trachyandesite, was chosen as the parent composition to model the liquid line of descent for successively more silica-rich samples in the alkali-rich subdivision (Table 4).

Table 4: Sequence 1 alkali-rich subdivision samples from the Wocus Bay quadrangle, Klamath County, Oregon.

Sample ID	**Lithology**	**SiO_2 (wt %)**	**Mg #**	**Mineralogy**
108	Hyaloclastite	--	--	Plag + FeTi + opx + cpx ± amph ± ap
46	Trachyte/ trachydacite	67.3	16	Plag + ol + opx
31	Trachydacite	64.5	25	Plag + ol + opx
44	Trachyandesite	61.1	34	Plag + ol + FeTi
67	Trachyandesite	57.6	41	Plag + cpx + FeTi
3	Trachyandesite	57.1	40	Plag + FeTi ± ol ± cpx
118	Basaltic trachyandesite	54.6	43	Plag + ol + FeTi ± cpx

Major element crystal fractionation model

The forward modeling program, COMAGMAT, was used to model the liquid line of descent for the major oxides. COMAGMAT is designed to model the liquid line of descent for major and trace elements for mafic suites (less evolved rocks); therefore, the program accounts for the crystallization of plagioclase, olivine, clinopyroxene, orthopyroxene, magnetite, and ilmenite. Because the most evolved alkali-rich samples crystallized amphibole and apatite phenocrysts, the geochemical trends for the alkalis (Na_2O and K_2O) can be overpredicted. CaO can be underpredicted because the program may crystallize more clinopyroxene than if amphibole were to crystallize. Element-element plots of these elements versus SiO_2

for the samples listed in Table 4 and the predicted compositions of COMAGMAT are shown on Figure 19, and in Appendices I and J.

COMAGMAT parameter selection

COMAGMAT allows the user to vary the oxygen fugacity, pressure, and water content of the parent composition. The TiO_2 and FeO compositional trends are primarily influenced by the oxygen fugacity; reducing conditions occur at low f_{O2} and oxidizing conditions occur at high f_{O2}. The quartz- magnetite-fayalite (QMF) buffer was used in the calculation and, therefore, the oxygen fugacity (log f_{O2}) varied from –3 to –12. Pressure was varied from 0.5 to 10 kbar which corresponds to minimum and maximum expected crustal depth; at P < 1.5 kbar, olivine crystallization begins, but the program discontinues when olivine crystallization ceases at 13 percent fractionation. The water content was varied from 0 to 2 weight percent. This range lies within the reported XRF unnormalized weight results for major and trace elements (**Error! Reference source not found.**); the total weight result for sample #118 (assumed parent) is 98.81 percent. This total allows for a maximum volatile content of the sample at 1.19 percent. In fact, the volatile content of the magma that produced this sample was probably higher. In either case, the variation in modeled water content from 0 to 2 weight percent falls within these limits. It is important to note that these parameters are interdependent. While the modeled liquid line of descent may work at other pressure, f_{O2}, and H_2O conditions, these conditions must make sense petrologically.

COMAGMAT results

The program begins to crystallize the assemblage plag (An_{55}) + aug + magn at log f_{O2} = -7.5 and –8, T = 1160 º C, P = 1.5 to 3 kbar (< 9 km), and H_2O < 0.4 weight percent. These results are displayed graphically in Figure 19 and in tabular form in **Error! Reference source not found.**. Results are displayed for maximum P and f_{O2} and H_2O = 0.2 weight percent in Figure 19. These conditions do not crystallize olivine, which is part of the parent assemblage. Therefore, results for P < 3 kbar and H_2O = 0.2 weight percent are displayed in Appendices I and J, and the only conditions that crystallize olivine in the fractionating assemblage are P < 2 kbar, f_{O2} < -8, and H_2O < 0.25 weight percent. However, these conditions fall within the ranges listed above.

COMAGMAT limitations

Because COMAGMAT is designed to model the liquid line of descent of major and trace elements in mafic suites, the program's applicability to model the felsic portion of the alkali-rich suite geochemical trends is limited. The alkali trends in combination with P_2O_5 are not accurately modeled because 1) the water content required to model the alkali concentrations is approximately 0.75 weight percent which is higher than the best fit solutions of < 0.4 weight percent H_2O for all other major elements, 2) crystallization of amphibole which incorporates potassium is not included in the program, and 3) crystallization of apatite which is needed to uptake phosphorous during fractionation. The liquid line of descent for CaO also yields a

poor fit because the program may crystallize more clinopyroxene than if amphibole was coprecipitating.

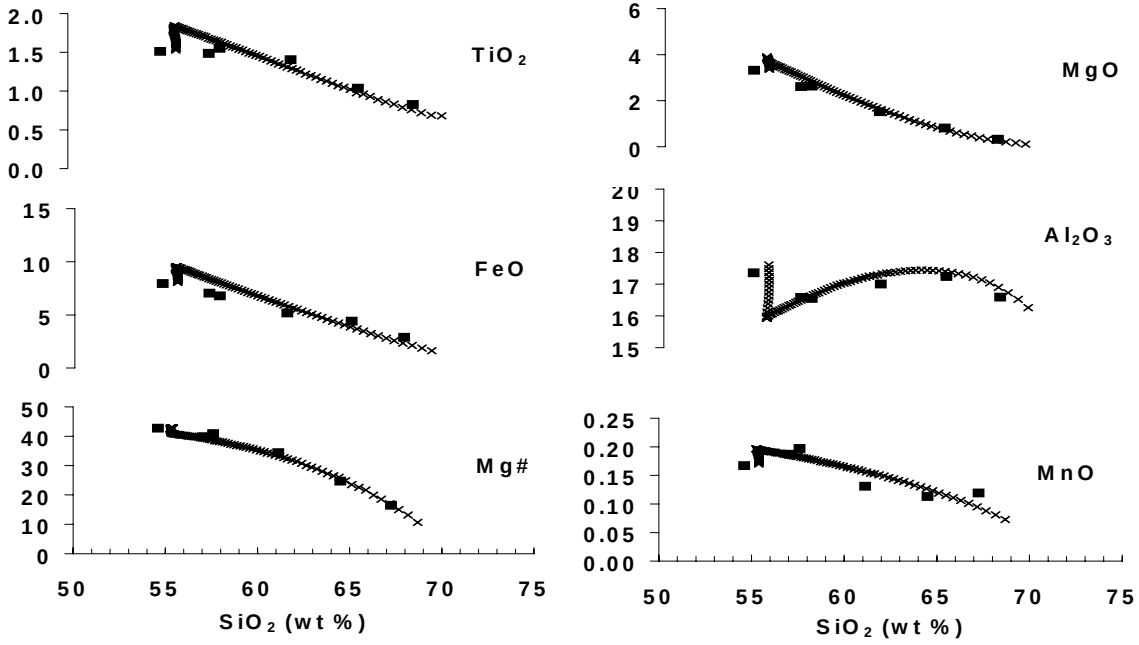

Figure 19: Oxide versus SiO_2 diagrams of sequence 1 alkali-rich samples (squares) and the predicted liquid lines of descent (x) modeled by COMAGMAT. P = 3 kbar, T = 1160 ºC, H_2O = 0.2 weight percent, log f_{O2} = -8 (QMF). At these conditions, plagioclase (initially An_{55}) crystallizes from 0 – 13 percent fractionation, plag + aug crystallize from 14 – 17 percent fractionation, and > 17 percent fractionation, the assemblage plag + aug + magn crystallizes. Mg # = 100 x [(MgO/40.31)/((MgO/40.31) + (FeO/71.85))]. All units are in weight percent. Data for model results presented in Appendix J.

Finally, the COMAGMAT results for the trace elements yield a poor fit to the observed geochemical trends because the program does not account for crystallization of two major phases in the most evolved samples of the alkali-rich suite that incorporate many incompatible trace elements (i.e., amphibole and apatite). Since the fractionating daughter assemblage is plag + magn + amph + opx + ap, the modeled concentrations of trace elements in the liquid line of descent are higher than the observed trace element trends.

Trace element crystal fractionation model

The trace element compositional trends of sequence 1 alkali-rich samples were modeled using the Rayleigh fractional crystallization equation $C_L/C_O = F^{(D-1)}$, where C_L = composition of the daughter liquid, C_O = composition of the parent liquid, F = fraction of remaining liquid, and D = partition coefficient. Rayleigh crystal fractionation is used as a basis for modeling the trace element patterns because it assumes perfect fractional crystallization in a closed chamber. Deviations from the model may then discussed in terms of other magmatic processes. Sample # 118, basaltic trachyandesite, was selected as the parent liquid composition (C_O), and samples # 46 and # 31 were selected as the range of fractionated daughter liquid compositions (C_L). The fraction of remaining liquid (F) was varied between 0 (0 % fractionation) and 1 (100 percent fractionation). The mineralogy was varied to reflect the change in mineralogy from the parental assemblage (plag + ol + cpx) to the daughter assemblage (plag + magn + amph + opx + ap). In addition, the mineral modes were varied within the following ranges as determined by petrography: 40-70

% plagioclase, 0-10 % magnetite, 0-27 % olivine, 0-36 % orthopyroxene, 0-26 % augite, 0-15 % amphibole (hbl), and 0-1 % apatite. Partition coefficients used are within the ranges of those reported in Grove and Donnelly-Nolan (1986) for Medicine Lake high-Na_2O andesites (Appendix K) and Wilson (1989) with noted exceptions. In some cases, the partition coefficient used was out of the ranges reported in these sources (± 1.00) in order to determine what the partition coefficient had to be to match the geochemical trends. In summary, the partition coefficients reported in Grove and Donnelly-Nolan (1986) and Wilson (1989) were used as starting point in the Rayleigh fractional crystallization equation.

The partition coefficient ranges presented in Grove and Donnelly-Nolan (1986) provide insight into the mineral phases that make up the dominant fractionating assemblage, and thus control the trace element composition of the daughter liquid. Table 5 details the key elements (as determined by the Rayleigh equation) incorporated into the mineral structures of the observed fractionating phases of the alkali-rich suite. In general, these elements have $D > 1$ for the appropriate phase.

When the ratio of the concentration of an element in the daughter liquid to the concentration of that element in the parent liquid (C_L/C_O) is plotted between 0 and 100 percent fractionation, the modeled C_L/C_O yields a best fit at approximately 50 percent fractionation for both the parent bulk mineral mode and the daughter bulk mineral mode (Figures 20 and 21). The 50 percent fractionation model also yields best fit curves for the individual mineral phases (Figure 22). Increasing percent

Table 5: Key elements incorporated into the structure of individual mineral phases of sequence 1 alkali-rich rocks as determined by the Rayleigh crystal fractionation trace element model (D > 1.00).

Mineral Phase	**Key elements incorporated into structure**
Plagioclase	Sr
Magnetite	Sc, Co, Cr, Ni
Olivine	Co, Cr, Ni
Augite	Sc, Co, Cr, Ni
Orthopyroxene	Sc, Co, Cr, Ni
Amphibole	Lu, Sc, Co, Cr, Ni
Apatite	La, Ce, Nd, Sm, Eu, Yb, Sr

fractionation causes the model C_L/C_O to shift up with greater Sr, Eu, Sc, Co, Cr, and Ni anomalies (i.e., the troughs increase in amplitude). Likewise, decreasing the percent fractionation flattens the model C_L/C_O and shifts the curve down. Therefore, the 50 percent fractionation curve best reproduces the observed fractionation trends with respect to both the values of C_L/C_O for trace elements and the peaks and troughs in the observed patterns.

D values for Sr, Eu, Sc, Co, Cr, and Ni are varied in Table 6 and on Figures 20 and 21 in order to maintain the best fit of the Rayleigh model curves for the various degrees of fractionation. These D values are varied because the single phase plots of Figure 22 indicate which elements are dominantly uptaken by the fractionating phases. For example, the troughs observed in Sr and Eu for the observed geochemical trends can be explained by fractionating plagioclase. Therefore, the D values for Sr and Eu are varied in the Rayleigh equation to maintain the best fit inside the troughs.

The modal mineralogy of the bulk parent and bulk daughter mineral modes shown in Figures 20 and 21 are the same mineral modes reported in Grove and Donnelly-Nolan (1986). These mineral modes provide the best fit for the 50 percent fractionation curve, and are consistent with petrographic observations. The abundance of amphibole is the only exception; Grove and Donnelly-Nolan (1986) reported 15 percent amphibole in the daughter mineral assemblage. This value is probably too high for the alkali-rich suite, as amphibole was one of the least abundant phases observed during petrographic analysis.

Magma mixing model

The role of magma mixing in the production of sequence 1 alkali-rich rocks was also explored (Appendix L). The mixing equation of Langmuir et al. (1978) for an element-element plot was used to plot major and trace elements versus weight percent SiO_2. The general form of the equation is $Ax + Bxy + Cy + D = 0$. On element-element plots, this mixing equation produces straight lines. The coefficients are defined by: $A = y_2 - y_1$, $B = 0$, $C = x_1 - x_2$, and $D = x_2y_1 - x_1y_2$. The endmembers of magma mixing used were sequence 2 HAOT and rhyolite. The rhyolite composition used in the equation: is a Pleistocene rhyolite from Newberry Volcano, sample N7-50 from Linneman (1990). The mixing lines between the Newberry rhyolite composition and the HAOT samples do not fit the sequence 1 alkali-rich trends for major and trace elements versus weight percent SiO_2 (Appendix L).

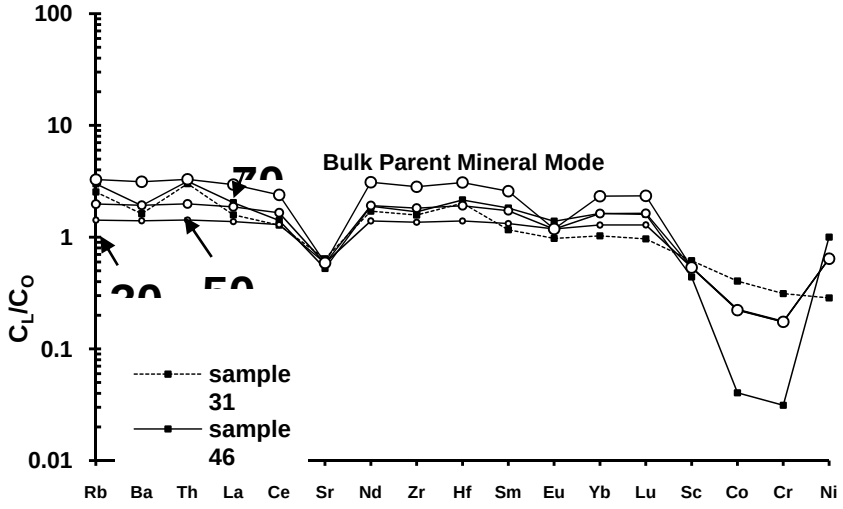

Figure 20: Rayleigh crystal fractionation model of trace elements for the parental bulk mineral mode (47% plagioclase, 27% olivine, 26% augite) of sequence 1 alkali-rich samples. Only model patterns for 30, 50, and 70 percent fractionation shown for simplicity. D values for Sr, Lu, Sc, Co, Cr, and Ni are listed in Table 6. Element order from Pearce and Parkinson (1993).

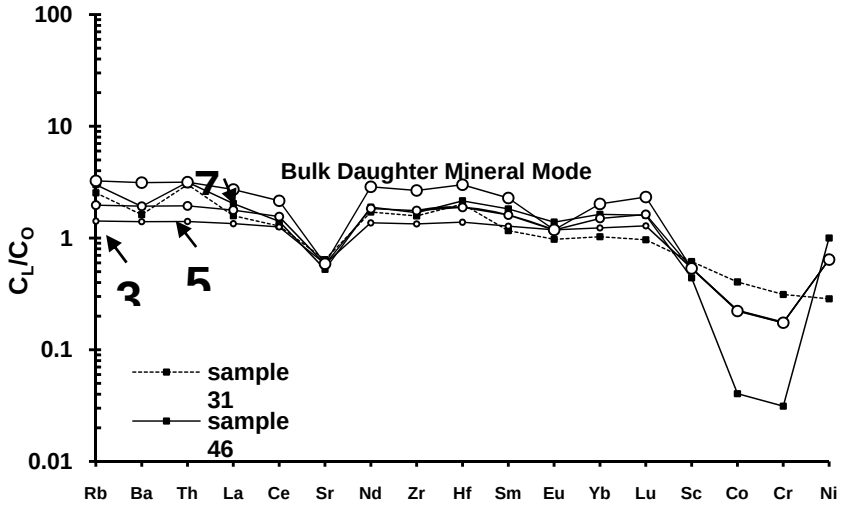

Figure 21: Rayleigh crystal fractionation model of trace elements for the daughter bulk mineral mode (69% plagioclase, 9.5% magnetite, 15% amphibole, 5.5% orthopyroxene, 1% apatite) of sequence 1 alkali-rich samples. Only model patterns for 30, 50, and 70 percent fractionation shown for simplicity. D values for Sr, Lu, Sc, Co, Cr, and Ni are listed in Table 6. Element order from Pearce and Parkinson (1993).

Table 6: Partition coefficient ranges for key trace elements in the fractionating mineral phases of sequence 1 alkali-rich samples. D value ranges taken from Grove and Donnelly-Nolan (1986) and D_{Ni} from Wilson (1989). Shaded cells correspond to D values that were varied to maintain best fit for the elements Sr, Eu, Sc, Co, Cr, and Ni.

	30% Fractionation	50% Fractionation	70% Fractionation
Plagioclase			
D_{Eu}	0.53	0.76	0.86
D_{Sr}	2.50	1.78	1.44
Amphibole			
D_{Lu}	1.00	1.00	1.00
D_{Sc}	2.75	1.90	1.52
D_{Co}	5.20	3.15	2.25
D_{Cr}	5.90	3.50	2.45
D_{Ni}	2.25	1.64	1.37
Augite			
D_{Sc}	2.75	1.90	1.52
D_{Co}	5.20	3.15	2.25
D_{Cr}	5.90	3.50	2.45
D_{Ni}	2.25	1.64	1.37
Magnetite			
D_{Sc}	2.75	1.90	1.52
D_{Co}	5.20	3.15	2.25
D_{Cr}	5.90	3.50	2.45
D_{Ni}	2.25	1.64	1.37
Orthopyroxene			
D_{Sc}	2.75	1.90	1.52
D_{Co}	5.20	3.15	2.25
D_{Cr}	5.90	3.50	2.45
D_{Ni}	2.25	1.64	1.37
Olivine			
D_{Co}	5.20	3.15	2.25
D_{Cr}	5.90	3.50	2.45
D_{Ni}	2.25	1.64	1.37

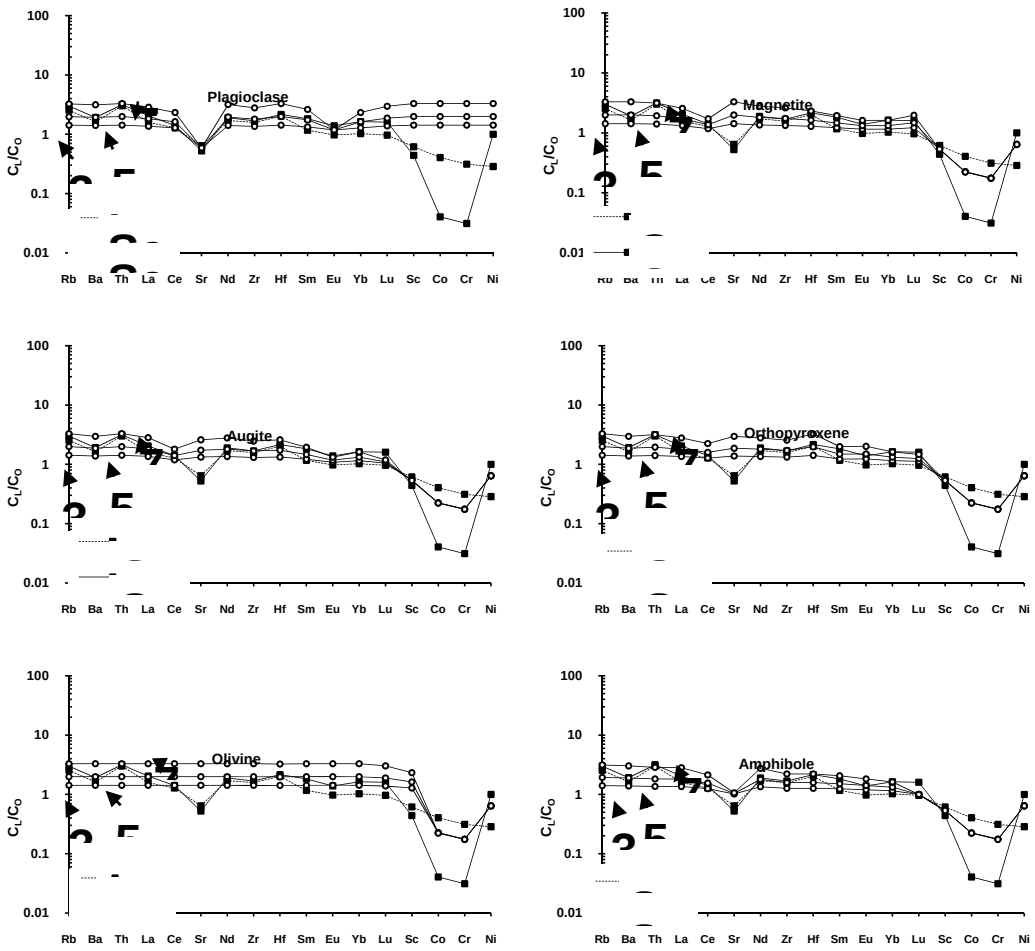

Figure 22: Rayleigh crystal fractionation model of trace elements for individual mineral phases of sequence 1 alkali-rich samples. Only model patterns for 30, 50, and 70 percent fractionation shown for simplicity. D values for Eu, Sr, Lu, Sc, Co, Cr, and Ni are listed in Table 6. Element order from Pearce and Parkinson (1993).

Contamination model

Crustal assimilation, or contamination, may also play a role in the production of sequence 1 alkali-rich rocks. The deviation in the observed concentrations of elements in the bulk parent and daughter mineral modes from the modeled concentrations in Figures 20 and 21, may be attributed to contamination. The Rayleigh crystal fractionation models for the bulk parent and daughter mineral modes

of sequence 1 alkali-rich rocks do not account for several observed trends in the trace elements (Figures 20 and 21). The best fit 50 percent fractionation curve does not account for Rb, Th, and Ce enrichment and Zr and HREE depletion in the observed data set. Therefore, a possible contaminant composition is LIL (Rb), Th, and LREE (~La, Ce) enriched, and HFSE (Zr) and HREE (Yb, Lu) depleted.

Sequence 2

Evaluation of primitive character

Sequence 2 rocks have previously been defined in the petrology section as HAOT based on compositional, textural and mineralogical parameters defined in Hart et al. (1984). HAOT are typically considered to be primitive; these lavas have had little modification since ascending from the mantle (Hart et al., 1984; Bailey and Conrey, 1992; Bacon et al., 1997; Conrey et al., 1997). Typically, HAOT have similar compositions to normal mid-ocean ridge basalts (N-MORB) (Bailey and Conrey, 1992; Bacon et al., 1997; Conrey et al., 1997). Given the geochemical and petrographic characteristics of HAOT in the vicinity of the Cascades and Basin and Range physiographic provinces outlined in Hart et al. (1984), Bailey and Conrey (1992), Bacon et al. (1997), Conrey et al. (1997), and Draper (1991), sequence 2 HAOT satisfy all criteria that define primitive HAOT highlighted in Table 8. For clarity, compositional data are listed in Table 9. Refer to the *Discussion* section for a detailed list of samples chosen for comparison.

Table 7: General characteristics of Cenozoic primitive HAOT in the vicinity of the Cascades and Basin and Range physiographic provinces in Oregon and northern California. Characteristics compiled from Hart et al. (1984), Draper (1991), Bailey and Conrey (1992), Bacon et al. (1997), Conrey et al. (1997). ol = olivine, cpx = clinopyroxene, plag = plagioclase, opx = orthopyroxene.

Characteristic	**Average HAOT**	**HAOT (this study)**
Modal mineralogy	ol ± cpx ± plag ± Cr-spinel	ol + cpx + opx + plag ± FeTi oxide
Texture	Diktytaxitic, nonporphyritic, subophytic to ophytic clinopyroxene, intergranular plagioclase	Diktytaxitic, nonporphyritic, subophytic to ophytic clinopyroxene and orthopyroxene, intergranular plagioclase
Average Mg#	> 60	65-68
Average TiO_2 (wt%)	≤ 1.35	1.162
Average K_2O (wt%)	≤ 0.39	0.14
Average Al_2O_3 (wt%)	> 16	17.77
Average MgO (wt%)	> 8.9	9.03
Average CaO (wt%)	10 - 12.5	11.24
HFSE	Slightly depleted relative to N-MORB	Slightly depleted relative to N-MORB
LIL	Enriched relative to N-MORB	Enriched relative to N-MORB
REE	Flat pattern, near 10x chondrite concentrations, slight HREE enrichment	Flat pattern, near 10x chondrite concentrations, slight HREE enrichment

Table 8: Average compositional data for sequence 2 HAOT, Medicine Lake HAOT (data from Bacon et al., 1997), Northern Cascades HAOT (data from Bailey and Conrey, 1992), HAOT of Hart et al. (1984), and N-MORB (data from Schilling et al., 1983). Major oxides in wt % and trace elements in ppm. Sequence 2 HAOT analyses by XRF, except REE analyses which are by INAA.

Element	N-MORB	Average HAOT (this study)	Average HAOT (Hart et al., 1984)	Northern Cascades HAOT	Medicine Lake HAOT
SiO_2	48.77	48.00	47.66	48.80	47.9
Al_2O_3	15.90	17.77	16.91	17.36	18.2
FeO*	9.82	9.49	9.88	8.95	8.94
MgO	9.67	9.03	9.06	9.27	9.40
CaO	11.16	11.24	11.20	11.96	11.3
Na_2O	2.43	2.84	2.53	2.37	2.46
K_2O	0.08	0.14	0.23	0.16	0.114
TiO_2	1.15	1.162	1.00	0.84	0.80
P_2O_5	0.09	0.139	0.13	0.10	0.07
MnO	0.17	0.177	0.17	0.18	0.16
Mg#	66.5	66.6	69.2	68.5	65.2
MgO/FeO*	0.98	0.95	0.92	1.04	1.05
La	2.10	2	--	3.10	2.65
Sm	2.74	1.6	--	1.97	1.90
Eu	1.06	0.60	--	0.81	0.83
Yb	3.20	2.2	--	2.65	2.19
Rb	0.56	1	2.1	2	--
Cs	0.007	1	--	--	0.028
Sr	88.7	310	255	201	255
Ba	4.2	94	141	76	79
Sc	40.02	36	--	44	40.8
V	262	232	191	247	202
Cr	528	169	--	313	213
Co	49.78	49	--	--	47.3
Ni	214	159	154	145	164
K/Rb	1547	1090	909	664	--
Rb/Sr	0.006	0.003	0.008	0.010	--

Discussion

The following section provides a discussion of the modeling results and implications presented in the geochemical modeling section. In particular, the magmatic processes acting to produce the alkali-rich lavas of sequence 1 and the HAOT of sequence 2 are developed, and a brief discussion of andesite production in the transition zone is also provided. The section is concluded with a chronology of the magmatic evolution of the six sequences and the interpreted tectonomagmatic processes that may be distinctive of the zone of transition.

Sequence 1 alkali-rich rocks produced by dry, shallow crystal fractionation

Liquid line of descent for alkali-rich sequence 1 rocks

Major and trace element modeling predicts relatively dry (< 0.4 wt % H_2O), shallow (< 9 km) fractionation of a basaltic trachyandesite magma with the assemblage plagioclase (An_{55}) + augite + magnetite to produce the trachyandesites and trachydacites with the assemblage plagioclase (An_{29}) + orthopyroxene + magnetite + amphibole + apatite. Approximately 50 percent fractionation accounts for observed trends in the alkali-rich rocks.

The mineral assemblage of parent sample #118 has phenocrystic olivine in thin section, and this is not predicted by COMAGMAT at H_2O > 0.20 weight percent. Petrographic analysis also confirms that olivine was not crystallizing as part of the parental fractionating assemblage; olivine phenocrysts in the basaltic trachyandesite parent are generally anhedral which indicates they were probably reacting with the melt. If the olivine phenocrysts were being resorbed, this would concur with the

results obtained from COMAGMAT which does not predict olivine in the fractionating assemblage. Conditions required to model the aug + plag + magn ± ol parent assemblage begin initially with crystallization of a relatively anhydrous (< 0.20 weight percent) magma. As the fractionation process continues, water content increases slightly (0.20 to 0.40 weight percent) changing the fractionating assemblage to plag + aug + magn (as modeled by COMAGMAT). This assemblage is seen in the trachyandesite intermediate daughter lavas (Table 4). Finally, olivine and augite disappear to form the daughter assemblage plag + opx + magn + amph + ap. Petrographic relationships of amphibole in the daughter lavas supports a dry, shallow fractionation model. Amphibole is only observed as pseudomorphous forms where it is completely altered to FeTi oxide, which suggests shallow anhydrous conditions, and possibly decompression.

Dry shallow fractionation of these lavas is consistent with the production of Na-rich andesitic to rhyolitic rocks at Medicine Lake, California and Volcán Ollagüe in the Andean central volcanic zone. Feeley and Hacker (1995) found that fractionation of a plagioclase-dominated mineral assemblage in shallow, vapor-absent crustal magma chambers produced Na-rich andesitic and dacitic magmas from a basaltic andesite parental magma at Volcán Ollagüe. Grove and Donnelly-Nolan (1986) also concluded that dry or shallow (< 6 km) crystallization (47 percent fractionation) produced high-Na_2O andesites at Medicine Lake. Medicine Lake lavas record the disappearance of olivine and augite (ol + aug + plag (An_{53}) parent assemblage) through reaction with the liquid to form the daughter assemblage

plagioclase (An_{30}), amphibole, orthopyroxene, magnetite, and apatite. The fractionation process of Na-rich lavas at Medicine Lake is very similar to the fractionation process determined for Na-rich rocks of sequence 1 in terms of anorthite content, degree of fractionation, mineral assemblages, and fractionation conditions (P, T, f_{O2}, weight percent H_2O). Medicine Lake high-SiO_2 and Na_2O andesite inclusions are aphyric with a plagioclase dominated mineral assemblage and oxide compositions indicate T = 1030 º C and log f_{O2} = -8.7.

Role of assimilation in the production of alkali-rich sequence 1 rocks

Assimilation of an Al_2O_3, TiO_2, LIL, LREE, and Th enriched, and a CaO, MgO, HFSE, HREE depleted contaminant would account for the discrepancies in the crystal fractionation models. Assimilation of a similar contaminant is discussed in Grove and Donnelly-Nolan (1986) for Medicine Lake parental andesite lavas. They conclude that crustal assimilation combined with different differentiation paths and variable water contents account for the compositional diversity of andesites and residual rhyolites at Medicine Lake. Feeley and Hacker (1995) also incorporate contamination into their shallow crustal differentiation model of basaltic andesite to andesite for Volcán Ollagüe. They contend that fractionation and contamination lower the density of basaltic andesite magma that is derived from deep silicic, garnet-bearing continental crustal chambers; the decrease in density allows the basaltic andesite magma to ascend to the base of andesitic chambers.

Sequence 2 HAOT produced by partial melting of peridotite

Comparison of sequence 2 HAOT to Cascades and Basin and Range HAOT

Sequence 2 HAOT may be compared to N-MORB and other HAOT in the vicinity of the study area to assess geochemical similarities and differences. These comparisons are summarized in Table 11.

The compositional data used in these comparisons come from four sources. Cascades HAOT refers to sample RCBD-41 from the northern Cascades in Conrey et al. (1997); sample RCBD-41 was selected because of its proximity to the study area and its geochemical similarity to sequence 2 HAOT. RCBD-41 is located at 45º05.67' N and 122º00.02' W. Sample 1376M was selected for its location (Medicine Lake Volcano) and its geochemical similarity to sequence 2 HAOT to represent the southern Cascades (Bacon et al., 1997). Basin and Range HAOT refers to HAOT from the northernmost Basin and Range (Draper, 1991), northern Basin and Range (Hart et al., 1984), and northwestern Basin and Range (McKee et al., 1983). These sources provide a range of HAOT compositions for that part of the Basin and Range that is nearest to the study area. The HAOT compositions obtained from Draper (1991) refer to samples NB219, NB235, NB319, NB271, NB265.1, NB263, NB326, NB275, and NB197 from along the Brothers Fault Zone (Draper, 1991); these samples are intended to represent the range of HAOT compositions for the Brothers Fault Zone, and thus part of the northernmost Basin and Range province as described in Draper (1991). Sample 50 (average HAOT composition) was selected from the northern Basin and Range (Hart et al., 1984). Sample 50 represents the

average composition of HAOT erupted in the northern Basin and Range province east of 122º W. Sample Alt-11 was selected to represent the northwestern Basin and Range from the Devil's Garden lava field (McKee et al., 1983). Alt-11 was selected for its proximity to the study area (41º 58.1' N and 120º 6.3' W) and its geochemical similarity to sequence 2 HAOT. Conclusions made regarding sequence 2 HAOT are based solely upon comparison with the reported data sets listed here.

LIL

All HAOT listed in Table 11 show LIL enrichment when compared to N-MORB. In particular, Ba and Sr are most markedly enriched in HAOT lavas. Sequence 2 HAOT have lower Ba (average 94 ppm) than Basin and Range HAOT (average 141 ppm), and higher concentrations than Cascades HAOT (~ 60-80 ppm). Sr in sequence 2 HAOT (average 310 ppm) is similar to Basin and Range HAOT (~ 200-324 ppm) and elevated when compared to Cascades HAOT (~ 255-265 ppm). However, the majority of samples for Basin and Range lie between 200 and 250 ppm for Sr; 324 ppm reported for Sr in the Devil's Garden sample is an outlier. The elevated Sr for sequence 2 HAOT is most similar to Sr concentrations found in basal HAOT lavas at Newberry (364-465 ppm) (Linneman, 1990). Sequence 2 HAOT Ba concentrations are also more similar to Newberry HAOT (130-215 ppm) than either the Basin and Range or the Cascades HAOT. The elevated Ba and Sr may be indicative of transition zone HAOT as these elevated concentrations of Ba and Sr are only found in HAOT erupted along the transition zone.

Table 9: Comparison of compositional data of selected HAOT relative to N-MORB and other HAOT. Bold-faced font is comparison of N-MORB to sequence 2 HAOT. Normal-faced font is comparison of selected HAOT to sequence 2 HAOT. Enriched = sequence 2 sample concentrations are higher than HAOT comparator, and depleted = sequence 2 HAOT sample concentrations are lower than HAOT comparator. 1. Data from Draper (1991). 2. Data from Hart et al. (1984). 3. Data from McKee et al. (1983), map no. Alt-11. 4. Data from Conrey et al. (1997), map # 3. 5. Data from Bacon et al. (1997), sample 1376M. 6. Data from Bailey and Conrey (1992). Number 6 HAOT from Powder River is included as a non-regional comparison.

Element Group	**HAOT sequence 2, Cascades-Basin and Range transition zone**	**1. Brothers Fault Zone HAOT Northernmost Basin and Range, central Oregon**	**2. HAOT Northern Basin and Range, southern Oregon**	**3. Devil's Garden HAOT Northwestern Basin and Range, south central Oregon**	**4. LKT Northern Cascades, 45º N, northern Oregon**	**5. Medicine Lake HAOT Southern Cascades, northern California**	**6. Powder River HAOT Northeastern Oregon**
LIL	**Enriched, Ba and Sr much higher**	**Enriched**	**Enriched**	**Enriched**	**Enriched**	**Enriched**	**Enriched**
		K and Rb enriched, Sr depleted	K, Rb, Ba enriched, Sr depleted	Enriched, Ba very enriched	K similar, Ba and Sr depleted, Rb enriched	K, Cs, Rb, Ba, Sr depleted	K, Sr and Ba depleted, Rb slightly enriched
HFSE	**Slightly depleted, V slightly depleted, Ti no change**	**Slightly depleted**	**Depleted**	**Depleted**	**Depleted**	**Depleted**	**Slightly depleted**
		Ta, Hf, Nb enriched, Zr depleted, Ti highly variable	Ti and V slightly depleted, Zr enriched	Ti and Zr very depleted	Zr and Nb enriched, Ti slightly depleted	Ti, V, Zr, Hf, Nb enriched, Ta depleted	Ti, Zr depleted, V, Nb, Ta, Hf enriched
REE	**Flat pattern near 10x chondrite, very slight**	**LREE enriched**	No data	**MREE and HREE depleted**	No data	**LREE enriched, Sm and Eu depleted**	**LREE enriched, MREE depleted**

	LREE enrichment	LREE enriched pattern 10-80x chondrite		REE enriched, more LREE enriched		LREE and MREE enriched	REE enriched, more LREE enriched
Compat-ibles	**Depleted, Cr much lower, Ni and Sc moderately lower, and Co no change**	**Depleted**	**Depleted**	**Depleted**	**Depleted**	**Depleted, Ni and Cr depleted, Co and Sc similar**	**Ni and Cr depleted, Sc enriched**
		Cr and Ni enriched, Sc no change	Ni similar	Ni enriched	Ni depleted, Cr and Sc enriched	Sc, Cr, Ni, Cu, Zn enriched, Co slightly depleted	Ni and Cu depleted, Cr and Sc enriched, Zn similar
MgO/ FeO*	**Slightly lower**	**Lower**	**Lower**	**Higher**	**Higher**	**Higher**	**Same**
		Lower	Lower	Higher	Higher	Higher	Higher
Mg#	**No change**	**Lower**	**Higher**	**Higher**	**Higher**	**Slightly lower**	**Higher**
		Lower	Higher	Higher	No data	Slightly lower	Higher
Major Oxides	**MnO and CaO similar, FeO* and MgO depleted, alkalis, Al_2O_3 and P_2O_5 enriched**	**MnO and CaO similar, FeO* enriched, MgO depleted, Na_2O slightly enriched, Al_2O_3 and P_2O_5 enriched**	**MnO and CaO similar, FeO* slightly enriched, MgO depleted, Na_2O similar, Al_2O_3 and P_2O_5 enriched**	**MnO depleted, CaO enriched, FeO* and MgO depleted, Na_2O depleted, Al_2O_3 and P_2O_5 enriched**	**MnO similar, CaO slightly enriched, FeO* and MgO depleted, Na_2O slightly enriched, P_2O_5 similar, Al_2O_3 enriched**	**MnO and CaO similar, FeO* and MgO depleted, Na_2O and P_20_5 similar, Al_2O_3 enriched**	**MnO and CaO enriched, FeO* and MgO depleted, Na_2O depleted, Al_2O_3 and P_2O_5 enriched**

		MnO similar, CaO depleted, FeO* slightly enriched, MgO similar, K_2O enriched, Na_2O depleted, Al_2O_3 depleted, P_2O_5 enriched	MnO and CaO similar, MgO similar, FeO* enriched, K_2O slightly enriched, Na_2O slightly depleted, Al_2O_3 depleted, P_2O_5 similar	MnO depleted, CaO enriched, FeO* depleted, MgO enriched, P_2O_5 enriched, Al_2O_3 and Na_2O enriched	MnO and Cao similar, FeO* depleted, MgO enriched, Na_2O, Al_2O_3 and P_2O_5 depleted	MnO and CaO similar, FeO* depleted, MgO enriched, Na_2O and P_2O_5 depleted, Al_2O_3 enriched	MnO similar, CaO slightly enriched, FeO* depleted, MgO enriched, Al_2O_3 and Na_2O depleted, P_2O_5 similar

HFSE

All HAOT listed in Table 11 are slightly to moderately HFSE depleted relative to N-MORB. Sequence 2 HAOT Ta (0.1-0.4 ppm), Nb (1-3 ppm), Hf (1-2 ppm) and V (224-248 ppm) are most similar to Cascades HAOT Ta (~ 0.11 ppm), Nb (1.3-2.7 ppm), Hf (~ 1.41), and V (202-217 ppm). Basin and Range HAOT have higher Ta (0.27-1.00 ppm), Nb (3.1-7.4 ppm), and Hf (1.1-3.6 ppm), and lower V (~ 191 ppm). Ti and Zr concentrations in sequence 2 HAOT (~ 1.16 weight percent and 74 ppm, respectively) are also similar to Cascades HAOT (~1.00 weight percent and 68-82 ppm, respectively). Ti and Zr concentrations are variable in Basin and Range HAOT lavas. Finally, sequence 2 HAOT HFSE concentrations are much lower than those for Pleistocene Newberry HAOT. Newberry HAOT HFSE concentrations more closely resemble Basin and Range HAOT HFSE, as they are both more variable and generally more HFSE enriched.

REE

All HAOT listed in Table 11 are LREE enriched relative to N-MORB. Sequence 2 HAOT REE patterns are relatively flat with very slight HREE enrichment and values near 10x chondrite. This pattern most closely resembles the REE pattern for Cascades HAOT. The patterns shown in Bacon et al. (1997) for Medicine Lake HAOT are also HREE enriched, and nearly flat at 10x chondrite. These patterns differ from Basin and Range REE patterns shown in Draper (1991). These lavas show mild LREE enrichment and values greater than 10x chondrite.

Major oxides and compatible elements

Major oxide compositions of the HAOT are very similar to N-MORB, with slight variability in FeO* and MgO concentrations. This is reflected in some general patterns observed with MgO/FeO*. MgO/FeO* = 0.98 for N-MORB; this ratio is lower for sequence 2 HAOT (~ 0.95), higher for Cascades HAOT (1.05-1.07), and variable for Basin and Range HAOT (0.92-1.03). All HAOT listed in Table 11 are depleted with respect to compatible elements when compared to N-MORB. Sequence 2 HAOT Ni (138-178 ppm), Cr (148-190 ppm), Sc (31-39 ppm), Co (45-55 ppm), and Zn (59-68 ppm) compare favorably to Cascades HAOT (Ni, 147-164 ppm, Cr, 213-272 ppm, Sc, 39-41 ppm, Co, ~ 47 ppm, and Zn, 63-65 ppm). All sequence 2 HAOT compatible elements are within the range of Cascades HAOT except Cr, which is moderately lower. Ni and Cr for sequence 2 HAOT lie within the ranges for Basin and Range HAOT, but Ni and Cr are variable, and Sc is slightly higher in sequence 2 HAOT.

Element ratios

The only noteworthy relationships observed are in Rb/Sr and La/Nb. Sequence 2 HAOT have Rb/Sr = 0.004. This is similar to N-MORB, which has 0.006. A low ratio typically indicates little modification of the magma since rifting from its source. Since sequence 2 HAOT is lower than N-MORB, the low ratio is a reflection of the elevated Sr content. Cascades HAOT have a low ratio (Rb/Sr = 0.008) and Basin and Range HAOT are slightly higher (Rb/Sr 0.008-0.015). La/Nb is very different for Cascades and Basin and Range HAOT, > 2 and < 1.1, respectively. Sequence 2

HAOT is within the range of Cascades HAOT with La/Nb = 2.35. More differences are shown by chondrite-normalized Ce/Yb = 0.71-0.76 for sequence 2 and Cascades HAOT, and Ce/Yb > 1 for Basin and Range HAOT. Finally, chondrite-normalized Y/Zr > 0.7 for sequence 2 and Cascades HAOT, and Y/Zr < 0.6 for Basin and Range HAOT.

Tectonic affinity of sequence 2 primitive HAOT

While most sequence 2 HAOT major oxides do not deviate much from the N-MORB composition, sequence 2 HAOT seem to follow geochemical patterns of Basin and Range HAOT in terms of MgO and FeO*. MgO/FeO* is < 1.00 for both of these HAOT types, but is > 1.00 for Cascades HAOT. Other major oxides behave similarly across all types of HAOT with slight variations in Na_2O and P_2O_5 presumably due to varying degrees of fractionation and other possible magmatic processes. Because major element characteristics of HAOT are so similar for all HAOT included in this study, trace element patterns and deviations from N-MORB and primitive mantle compositions are a better geochemical indicator of tectonic affinity.

The geochemical behavior of sequence 2 HAOT in terms of trace elements most closely resembles that of HAOT erupted along the Cascades. Basin and Range HAOT are more HFSE and LREE enriched, and have REE concentrations over 10x chondrite. Sequence 2 and Cascades HAOT have consistently lower HFSE concentrations and flatter REE patterns with slight HREE enrichment and values near 10x chondrite. Sequence 2 HAOT also follow Cascades HAOT compatible

element patterns; the concentrations of compatible elements are similar and have somewhat narrow ranges. These patterns differ from Basin and Range HAOT in that Basin and Range HAOT typically are more compatible element enriched and more variable. While sequence 2 LIL most resemble Cascades (including Medicine Lake) LIL, Ba and Sr concentrations for sequence 2 HAOT lie between Cascades and Basin and Range concentrations and are most similar to flank HAOT lavas found at Newberry Volcano. This divergent Ba and Sr behavior may be a geochemical signature of HAOT lavas erupted within the Cascades - Basin and Range transition zone.

These patterns are exemplified on Figure 23. This figure contains sequence 2 HAOT - normalized spiderdiagrams with the element ordering shown in Pearce and Parkinson (1993). When compared to northern Cascades and Basin and Range HAOT, plotted points for the southern Cascades most closely mimic the concentrations found in sequence 2 HAOT in terms of LIL (Ba, K), LREE (La, Ce), MREE (Sm, Eu), and major and compatible elements (Fe, Mg, Cr, Ni) (i.e., the plotted points lie closest to 1.00, see Appendix M for statistical analysis). HFSE (Ta, Nb) concentrations from the northern Cascades are nearest to the average concentrations of those elements for sequence 2 HAOT.

Generation of andesites along the transition zone

By far, the greatest volume of volcanic rocks in the study area are of andesitic composition. They range in age from early Pliocene (3.5 – 4.5 Ma, sequence 1), to the early Pleistocene (approximately 1.1 Ma, sequence 6). Texturally, these andesites

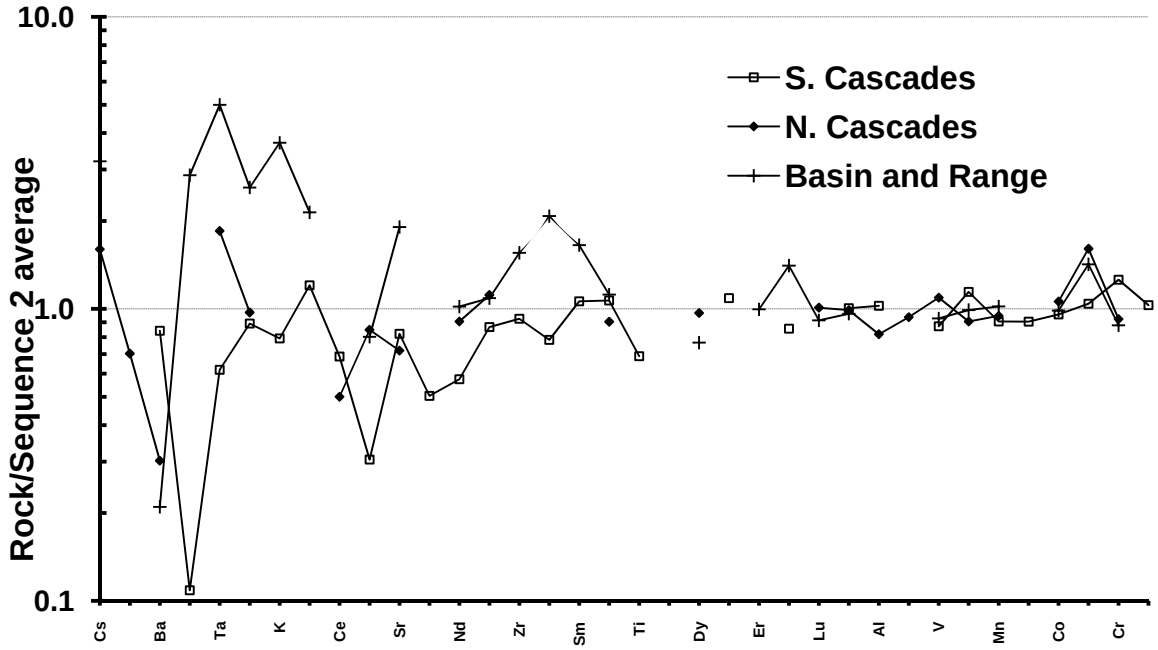

Figure 23: Sequence 2 HAOT-normalized spiderdiagrams comparing Cascades and Basin and Range HAOT to sequence 2 HAOT. Data for southern Cascades from Medicine Lake Volcano, sample 1376M (Bacon et al., 1997). Data for northern Cascades, sample RCBD-41 (Conrey et al., 1997). Data for Basin and Range are average concentrations calculated from samples NB319 and NB326 (Draper, 1991). Element ordering from Pearce and Parkinson (1993).

are generally porphyritic or microporphyritic, but to a lesser degree may be trachytic, aphanitic and rarely seriate (Table 3). Geochemically, the andesites are characterized by their variability (as opposed to HAOT or alkalic samples) on classification diagrams, element-element plots, and REE diagrams (Figures 6 to 18, Appendix G).

Multiple magmatic processes are most likely responsible for the production of andesite in the study area. Incompatible element enrichment and compatible element depletion patterns are observed in the geochemical patterns of sequence 4 rocks from Soloman Butte. These patterns are present on element-element plots and may imply crystal fractionation (Figure 15, Appendix G). Magma mixing textures are seen in many of the younger andesites where there are multiple populations of plagioclase phenocrysts. In addition, many of the younger andesites tend to be alkali, LIL, and Th enriched which may indicate crustal contamination, as discussed in the geochemical modeling section.

Combined crystal fractionation, magma mixing, and assimilation processes have been described by Grove et al. (1982) for calc-alkalic andesite lavas at Medicine Lake Volcano. Grove et al. (1982) discuss a combination of these processes acting to produce calc-alkaline series lavas during Pleistocene and Holocene time. They describe an initial high-alumina basalt (HAB) magma rising through the lower crust with no assimilation or mixing. When the HAB magma reaches upper crustal levels, the magma begins to undergo crystal fractionation. Magma-wallrock interactions initiate crustal assimilation. Density differences cause

stratification of the magma chamber. The silicic cap and fractionated HAB daughter magma mix producing lavas from basaltic andesite to rhyolite.

Magmatic evolution of the sequences

Alkalic lavas

From approximately 3.5 to 4.5 Ma, the Cascades - Basin and Range transition zone in the vicinity of 43º N was dominated by the two interfingering volcanic suites of sequence 1; in the alkali-rich suite, trachyandesite, trachydacite and trachyte daughter lavas were likely produced by dry shallow fractionation of a basaltic trachyandesite parental magma. These lavas may have been contaminated by a LIL, LREE, and Thenriched, and a HFSE, HREE depleted crustal contaminant during differentiation. In the other suite, the low-alkali basaltic andesite and andesite lavas shift from tholeiitic to calc-alkalic compositions upsection.

The production of compositionally diverse andesitic lavas (i.e., alkalic, subalkalic) by combined processes of batch melting, fractionation, and crustal assimilation has been discussed by Grove and Donnelly-Nolan (1986) for Medicine Lake lavas. They conclude that Medicine Lake andesite lavas followed different differentiation paths due to variable water contents of different parent magma batches. Some magmas rise to shallow levels and undergo fractionation under relatively anhydrous conditions producing Na_2O-rich andesite. Such a scenario has been developed for the alkali-rich suite of sequence 1. Likewise, low-Na_2O andesite is produced by wet and deeper crystallization, which may be analogous to the low-alkali suite of sequence 1. Since variable water content is interpreted by Grove and

Donnelly-Nolan (1986) as different parental magma batches, the alkali-rich and low-alkali suites of sequence 1 may also represent different magma batches.

During the Pleistocene, multiple interfingered calc-alkalic andesite and trachyandesite lava flows were erupted. Some of the younger andesite lava flows have geochemical and textural characteristics similar to the alkali-rich lavas of sequence 1, although Al_2O_3 and Sr concentrations in sequence 6 lava flows are considerably higher. The trachytic texture and geochemical characteristics of the andesite/trachyandesite lava flows suggest they were produced by magmatic processes similar to those producing sequence 1 alkali-rich lava flows, although sequence 6 lavas show magma mixing textures. Sequence 6 andesite/trachyandesite lava flows most likely underwent similar magmatic processes to those modeled for the alkali-rich suite of sequence 1, although the higher Al_2O_3 content indicates a higher water content in the parental lava. In addition, the higher Sr content indicates less plagioclase and apatite control during fractionation. This is supported by the slight positive Eu anomalies displayed in the REE patterns of sequence 6 samples; a positive Eu anomaly indicates less uptake of Eu by plagioclase and apatite during fractionation, or addition of plagioclase to the magma during mixing events. However, positive Eu anomalies can be enhanced or created by an abundance of Eu in the magma. While magma mixing was not found to be a magmatic process in the production of the alkalic lavas of sequence 1, mixing is indicated for the sequence 6 andesite and trachyandesite lavas. Multiple plagioclase phenocryst populations,

complex zoning patterns, reaction rims and overgrowths are considered to be mixing textures.

In summary, the alkalic lavas of sequence 1 and 6 imply the combined magmatic processes of fractionation, assimilation, mixing, and batch melting. Parent magmas of sequence 1 lavas may have had variable water contents causing daughter magma batches to crystallize at deeper (subalkalic lavas) and shallower levels (alkalic lavas). Subsequent fractionation and crustal contamination produced the alkalic lavas, and similar processes combined with magma mixing likely produced the andesite and trachyandesite lavas of sequence 6 as well.

HAOT and HAB lavas

At approximately 3.0 Ma, the primitive HAOT lava flows of sequence 2 were erupted. The primitive nature of these lavas indicates that they moved through the crust quickly with little to no ponding. Such primitive lavas have erupted over millions of years in Oregon. Hart et al. (1984) discuss primitive HAOT erupted in the late Miocene (10.5 Ma) to the mid-Holocene, McKee et al. (1983) describe primitive HAOT at Devil's Garden lava field (approximately 5-10 Ma), Draper (1991) describes primitive HAOT along the Brothers Fault Zone (Pliocene and Pleistocene), Linneman (1990) describes primitive HAOT flank lavas at Newberry Volcano, and Bacon et al. (1997) describe primitive HAOT at several Cascade volcanic fields including Crater Lake and Medicine Lake (Holocene). Primitive HAOT lavas have persisted from the Cascades through the transition zone and throughout the northern Basin and Range during the Neogene and Quaternary. These lavas show that

extension-dominated tectonics has allowed these lavas to erupt with very little if any interaction with the crust.

At approximately the Plio-Pleistocene boundary, sequence 5 tholeiitic HAB lava flows were erupted. These lavas are geochemically more evolved than the HAOT of sequence 2. Sequence 5 lava flows show more compatible element depletion and incompatible element enrichment than sequence 2 HAOT. These HAB are not primitive lavas. The HAB may follow a normal compositional fractionation trend on element-element plots, but this conclusion cannot be fully supported due to the low number of sample points. Elevated Th, Rb, and alkalis in the HAB lavas may indicate a crustal signature. The higher alkali content offsets these lavas from a possible liquid line of descent with the HAOT in Figure 5.

One interesting aspect of the sequence 5 HAB geochemistry is the Eu behavior. These samples show distinct negative and positive Eu anomalies on REE diagrams. The negative Eu anomalies may be caused by the uptake of Eu by plagioclase and apatite during fractionation. While distinct positive Eu anomalies may be explained by an excess amount of Eu in a magma, Prueher and McBirney (1988) conclude that addition of plagioclase to a magma during mixing events also produces strong positive Eu anomalies. Prueher and McBirney (1988) concluded that plagioclase was added to parental magmas of basalt-andesite sequences produced at cinder cones associated with the late stages of activity at Crater Lake. They concluded that each successive basalt-andesite sequence underwent magma mixing and subsequent fractionation. Major and trace element variations show a decrease in compatible

elements and an increase in incompatible elements consistent with fractionation of the assemblage olivine + plagioclase + clinopyroxene + orthopyroxene + magnetite. Since plagioclase fractionation is viewed as a viable process, they explain the strong positive Eu anomalies as being produced by the addition of plagioclase during mixing events. Addition of plagioclase during mixing events might be a plausible explanation for the observed strong positive Eu anomalies of sequence 5 HAB. Petrographic analysis supports a magma mixing hypothesis in that plagioclase phenocrysts exhibit complex zoning and have inclusions. Prueher and McBirney (1988) also conclude that the basalt-andesite sequences of cinder cones associated with Crater Lake have more than one parent magma. This conclusion is supported by increasing LREE enrichment of successive basalt-andesite sequences.

In summary, the HAOT and HAB lavas imply multiple magmatic processes. HAOT lavas maintain a primitive geochemical signature as they are able rise to the surface with little to no interaction with the crust. HAB lavas show a more evolved geochemical signature whereby they may undergo fractionation, assimilation, and magma mixing. Further study of the HAB lavas may also indicate that these lavas have more than one parent magma.

Andesitic lavas

From approximately 3.5 to 4.5 Ma, the low-alkali suite of basaltic andesite lavas of sequence 1 were erupted. Batch melting was explored as a likely process for the production of these lavas in an earlier section. In addition, these lavas may have

also been produced via magma mixing as complex zoning patterns and multiple populations of plagioclase phenocrysts are seen in thin section.

At about the same time as the sequence 1 low-alkali lavas were erupted, the Yamsay Mountain volcanic complex was forming to the east. Hering (1981) concluded that intense mafic volcanism and extensional tectonics facilitate melting, leading to the development of the basaltic andesite and silicic lavas at Yamsay Mountain. He describes discrete partial melting events as the process by which the basaltic andesite lavas were produced. In addition, he finds that the silicic lavas were produced by fractionation of a dacitic parent magma. Such magmatic processes most likely produced the low-alkali suites of sequence 1. Since the low-alkali basaltic andesite lavas vary considerably in texture and geochemistry, these lavas may have been produced by the combined processes of partial melting and subsequent fractionation. This hypothesis may be evaluated as more data become available.

From approximately 2.5 to 2.0 Ma, calc-alkalic basaltic andesite and andesite lava flows form the composite volcano at Soloman Butte and basaltic andesite lava flows erupted to the east of Soloman Butte. The earlier basaltic andesite lava flows (sequence 3) and Soloman-type andesites (sequence 4) show evidence of combined assimilation, crystal fractionation and magma mixing processes.

The major and trace element pattern in sequence 3 basaltic andesite lava flows follow a normal compositional fractionation trend upsection. The earliest flow lies on the calc-alkalic/tholeiitic boundary in Figure 7, while later lava flows lie within the calc-alkaline field. However, petrographically, textural characteristics suggest

magma mixing in addition to magmatic differentiation. All lava flows have multiple plagioclase populations including large blocky phenocrysts, smaller prismatic phenocrysts, and/or groundmass laths. Many plagioclase phenocrysts display swallow tails and secondary alteration reaction rims.

Soloman Butte (sequence 4) samples generally show incompatible element enrichment and compatible element depletion trends with respect to increasing increasing silica content with exceptions listed below. While these geochemical trends suggest crystal fractionation, incompatible element trends and textural characteristics indicate magma mixing and/or contamination. LIL, HFSE, and REE concentrations decrease with increasing silica; these trends may be explained by a LIL, HFSE, and REE depleted contaminant, or mixing with a magma of similar signature. In addition, earlier basaltic andesite lava flows display negative Eu anomalies on chondrite-normalized REE diagrams, while later andesite lava flows display positive Eu anomalies. This trend might be explained by uptake of Eu by plagioclase and apatite during fractionation in the older lava flows, followed by an increase of Eu in younger lavas presumably due to magma mixing and/or contamination. However, since Eu occurs in two oxidation states, positive Eu anomalies may be produced by the abundance of Eu^{3+}. Mixing processes are also indicated by multiple plagioclase and olivine phenocryst populations in all Soloman Butte lava flows. Plagioclase phenocrysts give many lava flows a seriate texture, and some of these phenocrysts display reverse compositional zoning and secondary alteration rims. In addition, olivine phenocrysts form two textures: either highly

fractured, skeletal grains with intense secondary alteration, or subhedral to euhedral forms with very minor secondary alteration.

During the Pleistocene, multiple calc-alkalic basaltic andesite lavas of sequence 6 were erupted. These lavas vary considerably in texture and geochemistry, and the only magmatic process implied by petrologic analysis is magma mixing. As with the other andesitic lavas discussed, these lava flows have multiple plagioclase phenocryst populations, complex zoning patterns and abundant inclusions. Other magmatic processes will likely be suggested as more data become available.

In summary, the andesitic lavas of sequences 1, 3, 4, and 6 were probably produced by fractionation, contamination, mixing, and batch melting. These processes have classically been associated with the production of andesites in a volcanic arc environment. Because the andesite lavas of this study are so variable in texture and geochemistry, modeling of these lavas is beyond the scope of this project. While geochemical patterns on element-element plots and petrographic analysis suggest fractionation, contamination, and magma mixing, further study of these rocks is required to draw heartier conclusions.

Tectonomagmatic synthesis and summary

The immediate back-arc of the Cascade Range during the Pliocene and Pleistocene produced spatially and temporally varied lavas including HAOT, alkali-rich trachytic suites, HAB, and a variety of andesitic compositions. These diverse chemical types reflect an array of magmatic processes that may be distinctive to the transition zone that lies between the Cascades and Basin and Range provinces.

Within this zone, magmas were able to rise to the surface with little ponding as demonstrated by the lavas of sequence 2 (HAOT) and sequence 5 (HAB). Geochemical patterns of the primitive HAOT indicate these lavas are more closely related to subduction zone primitive HAOT lavas, rather than primitive HAOT erupted in the Basin and Range province. These sequences suggest extension-dominated tectonics that allowed magmas to rise unimpeded during the late Pliocene and early Pleistocene. However, similar conditions may be inferred for the early to middle Pliocene as primitive HAOT persist through time (at least 10.5 to 0 Ma) in the neighboring Cascades and Basin and Range provinces. In addition, elevated LIL (Ba, Sr) concentrations may be indicative of transition zone HAOT and warrants further study.

Geochemical modeling of the alkali-rich lavas indicates their parental magmas were able to move through the crust to shallow levels (< 9 km) before experiencing magmatic differentiation and crustal assimilation. Alkali-rich suites seem to occur throughout time along the transition zone. They have been described at Medicine Lake (Holocene), in the Bryant Mountain and Langell Valley quadrangles (8.18 ± 0.12 Ma) (Jenks, in prep.), and in this study (3.5 – 4.5 Ma).

Production of alkali-rich and low-alkali suites of sequence 1 might be explained by multiple parental magma batches with variable water contents. Dry parent magmas result in alkali-rich suites, while wet parent magmas result in low-alkali suites. Batch melting and magma mixing may also be responsible for the textural and compositional diversity of transition zone andesite. Andesitic lavas from

many volcanic fields in the transition zone, including those studied here, have classically been viewed as the products of combined magmatic processes (i.e., fractionation, assimilation, mixing, batch melting).

Characterization of the Cascades – Basin and Range transition zone may be summarized by the occurrence of various rock types generated by multiple magmatic processes through time. Specifically, HAOT, HAB, alkali-rich suites, and andesite occur together; therefore, the magmatic processes thought to produce these various rock types also occur together (i.e., magma mixing, fractionation, assimilation, partial melting, batch melting). The other very important aspect of this conclusion is that these processes persist through time. It may be that the transition zone is characterized by the ongoing occurrence of multiple magmatic processes and extension-dominated tectonics.

References Cited

Ariskin, A. A., 1992, COMAGMAT software version 3.0; complex of programs to solve igneous petrology problems: Moscow, Russia.

Bacon, C. R., Bruggman, P. E., Christiansen, R. L., Clynne, M. A., Donnelly-Nolan, J. M., Hildreth, W., 1997, Primitive magmas at five Cascade volcanic fields: melts from hot, heterogeneous sub-arc mantle: The Canadian Mineralogist, v. 35, p. 397-423.

Bacon, C. R., Lanphere, M. A., Champion, D. E., 1999, Late Quaternary slip rate and seismic hazards of the West Klamath Lake fault zone near Crater Lake, Oregon Cascades: Geology, v. 27, no. 1, p. 43-46.

Bailey, D. G. and Conrey, R. M., 1992, Common parent magma for Miocene to Holocene mafic volcanism in the northwestern United States: Geology, v. 20, p. 1131-1134.

Beyer, R. L., 1973, Magma differentiation at Newberry Crater in central Oregon [Ph. D. thesis]: University of Oregon, 93 p.

Bolton, L. J., Uzzelle, G. H., Cross, J. B., Dennis, A. J., 1997, Geology of the Modoc Zone in the Colliers 7.5' Quadrangle S. C.: Geological Society of America Abstracts with Programs, v. 29, no. 3, p. 6.

Brikowski, T. H., 1983, Chemical variation across the Cascade volcanic arc in southern Oregon: Eos, Transactions, American Geophysical Union, v. 64, no. 45, p. 900.

Bullen, T. D., 1983, Evidence for chemical and mineralogical heterogeneity in the source region of northeastern California basalts: Geological Society of America Abstracts with Programs, v. 15, no. 6, p. 536.

Bullen, T. D., 1984, Evidence against crystal fractionation from basalt as a mechanism for generation of N. E. California andesites: Geological Society of America Abstracts with Programs, v. 16, no. 6, p. 458.

Bullen, T. D., 1986, Magmagenesis in the Devil's Garden lava field; implications for the nature of the subcontinental lithosphere at an active continental margin [Ph. D. thesis]: Univeristy of California, Santa Cruz, 354 p.

Carlson, R. W. and Hart, W. K., 1990, Westward migration of calc-alkaline basaltic volcanism and the nature of the Cascades - Basin and Range Boundary: Eos, Transactions, American Geophysical Union, v. 71, no. 43, p. 1607.

Catchings, R. D., 1990, Seismic implications for crustal composition and deformation along the Basin and Range/Cascade Range boundary: Eos, Transactions, American Geophysical Union, v. 71, no. 43, p. 1613.

Conaway, J. S., 2000, Hydrogeology and paleohydrology in the Williamson River Basin, Klamath County, Oregon [M. S. thesis]: Portland State University, 117 p.

Conaway, J. S. and Cummings, M. L., in press, Geology of the Wocus Bay quadrangle, Klamath County, Oregon: Oregon Department of Geology and Mineral Industries GMS-?, scale 1: 24,000.

Conrey, R. M., Sherrod, D. R., Hooper, P. R., Swanson, D. A., 1997, Diverse primitive magmas in the Cascade Arc, northern Oregon and southern Washington: The Canadian Mineralogist, v. 35, p. 367-396.

De La Fuente, J. and Tatman, D., 1991, Geology of Klamath National Forest: National Speleological Society Bulletin, v. 53, no. 1, p. 56.

DePaolo, D. J., 1981, Trace element and isotopic effects of combined wallrock assimilation and fractional crystallisation: Earth and Planetary Science Letters, v. 53, p. 189-202.

Devey, C. W., Garbe-Schönberg, C. D., Stoffers, P., Chauvel, C., Mertz, D. F., 1994, Geochemical effects of dynamic melting beneath ridges: reconciling major and trace element variations in Kolbeinsey (and global) mid-ocean ridge basalt: Journal of Geophysical Research, v. 99, p. 9077-9095.

Donnelly-Nolan, J. M., 1988, A magmatic model of Medicine Lake Volcano, California: Journal of Geophysical Research, v. 93, no. 5, p. 4412-4420.

Donnelly-Nolan, J., 1990, Geology of Medicine Lake Volcano, Northern California, Cascade Range: Geothermal Resources Council Transactions, v. 14, no. part II, p. 1395.

Draper, D. S., 1991, Late Cenozoic bimodal magmatism in the northern Basin and Range Province of southeastern Oregon: Journal of Volcanology and Geothermal Research, v. 47, p. 299-328.

Dzurisin, D., Donnelly-Nolan, J. M., Evans, J. R., Walters, S. R., 1990, Relation between magmatism and tectonism near Medicine Lake Volcano, California,

inferred from historical subsidence, seismicity, and crustal structure: Eos, Transactions, American Geophysical Union, v. 71, no. 43, p. 1608.

Eggins, S. M., 1992, Petrogenesis of Hawaiian tholeiites. 2. Aspects of dynamic melt segregation: Contributions to Mineralogy and Petrology, v. 110, p. 398-410.

Elliot, T. R., Hawkesworth, C. J., Grönvold, K., 1991, Dynamic melting of the Iceland plume: Nature, v. 351, p. 201-206.

England, D. L., 1987, Geology in the Modoc Pb-Ag-Zn district, Inyo County, California [M. S. thesis]: University of Minnesota, 82 p.

Feeley, T. C. and Hacker, M., 1995, Intracrustal derivation of Na-rich andesitic and dacitic magmas: an example from Volcán Ollagüe, Andean Central Volcanic Zone: Journal of Geology, v. 103, p. 213-216.

Gardner, J. E., Carey, S., Sigurdsson, H., 1998, Plinian eruptions at Glacier Peak and Newberry volcanoes, United States: Implications for volcanic hazards in the Cascade Range: Geological Society of America Bulletin, v. 110, no. 2, p. 173-187.

Gerlach, D. C., Sando, T. W., Grove, T. L., 1981, Petrogenesis of calc-alkaline rocks at Medicine Lake Highland, California; geochemical evidence: Eos, Transactions, American Geophysical Union, v. 62, no. 45, p. 1086.

Gerlach, D. C. and Grove, T. L., 1982, Petrology of Medicine Lake Highland volcanics; characterization of endmembers of mixing: Contributions to Mineralogy and Petrology, v. 80, no. 2, p. 145-159.

Grose, T. L. T., Saucedo, G. J., Wagner, D. L., 1990, Cascade-Basin & Range transition east of Lassen Peak: Eos, Transactions, American Geophysical Union, v. 71, no. 43, p. 1613.

Grove, T. L., Gerlach, D. C., Sando, T. W., 1981, The role of combined assimilation, fractionation, and mixing in the production of calc-alkaline series magmas: Eos, Transactions, American Geophysical Union, v. 62, no. 45, p. 1086.

Grove, T. L., Gerlach, D. C., Sando, T. W., 1982, Origin of calc-alkaline series lavas at Medicine Lake Volcano by fractionation, assimilation and mixing: Contributions to Mineralogy and Petrology, v. 80, no. 2, p. 160-182.

Grove, T. L., Gerlach, D. C., Sando, T. W., Baker, M. B., 1983, Origin of calc-alkaline series lavas at Medicine Lake Volcano by fractionation, assimilation and mixing; corrections and clarifications: Contributions to Mineralogy and Petrology, v. 82, no. 4, p. 407-408.

Grove, T. L. and Baker, M. B., 1984, Phase equilibrium controls on the tholeiitic versus calc-alkaline differentiation trends: Journal of Geophysical Research, v. 89, no. B5, p. 3253-3274.

Grove, T. L. and Donnelly-Nolan, J. M., 1986, The evolution of young silicic lavas at Medicine Lake Volcano, California: Implications for the origin of composition gaps in calc-alkaline series lavas: Contributions to Mineralogy and Petrology, v. 92, p. 281-302.

Grove, T. L., Baker, M. B., Kinzler, R. J., Donnelly-Nolan, J. M., 1986, Mineralogical evidence of magmatic processes at Medicine Lake Highland, N. California; a convergent margin calc-alkaline volcanic system: Papers and Proceedings of the General Meeting - International Mineralogical Association, p. 115-116.

Guffanti, M. and Weaver, C. S., 1988, Distribution of Late Cenozoic volcanic vents in the Cascade Range: Volcanic arc segmentation and regional tectonic considerations: Journal of Geophysical Research, v. 93, no. B6, p. 6513-6529.

Gunn, B. M. and Watkins, N. D., 1970, Geochemistry of the Steens Mountain basalts, Oregon: Geological Society of America Bulletin, v. 81, no. 5, p. 1497-1515.

Gunn, S. H., Conrey, R. M., Sherrod, D. R., 1996, Sr, Pb and Nd isotopic study of Cascade Range basalts in northern Oregon: constraints on mantle heterogeneity in a subduction zone: Geological Society of America Abstracts with Programs, v. 28, p. 71.

Hart, W. K., Aronson, J. L., Mertzman, S. A., 1984, Areal distribution of low-K, high-alumina olivine tholeiite magmatism in the northwestern Great Basin: Geological Society of America Bulletin, v. 95, p. 186-195.

Hart, W. K., 1985, Chemical and isotopic evidence for mixing between depleted and enriched mantle, northwestern U. S. A.: Geochimica et Cosmochimica Acta, v. 49, p. 131-144.

Hawkesworth, C., Turner, S., Gallagher, K., Hunter, A., Bradshaw, T., Rogers, N., 1995, Calc-alkaline magmatism, lithospheric thinning and extension in the Basin and Range: Journal of Geophysical Research, v. 100, no. B7, p. 10,271-10,286.

Hering, C. W., 1981, Geology and petrology of the Yamsay Mountain complex, South-Central Oregon: A study of bimodal volcanism [Ph. D. thesis]: University of Oregon, 194 p.

Hermance, J. F., 1990, Tectonic implications of the deep electrical conductivity structure of the Cascades/Basin and Range transition in central Oregon: Eos, Transactions, American Geophysical Union, v. 71, no. 43, p. 1607-1608.

Higgins, M. W., 1968, The geology of Newberry Caldera, central Oregon [Ph. D. thesis]: University of California, Santa Barbara, 320 p.

Higgins, M. W., 1973, Petrology of Newberry Volcano, Central Oregon: Geological Society of America Bulletin, v. 84, no. 2, p. 455-487.

Hooper, P. R., Bailey, D. G., Holder, G. A., Urbanzcyk, K. M., 1993, Calc-alkaline magmatism associated with lithospheric extension in the Eocene and Miocene of the Pacific Northwest, U. S. A.: Geological Society of America Abstracts with Programs, v. 25, no. 4, p. 54.

Illian, J. R., 1970, Interim report on the ground water in the Klamath Basin, Oregon, State Engineer, 110 p.

Irvine, T. N. and Baragar, W. R. A., 1971, A guide to the chemical classification of the common rocks: Canadian Journal of Earth Science, v. 8, p. 523-548.

Jenks, Margaret D., in prep., Preliminary geologic map of the Bryant Mountain and Langell Valley quadrangles, Klamath County, Oregon: Oregon Department of Geology and Mineral Industries GMS-?, scale 1:24,000.

Jensen, R. A., 1988, Roadside guide to the geology of Newberry Volcano: Bend, OR, Central Oregon Geology Publication, 75 p.

Keith, T. E. C. and Bargar, K. E., 1988, Petrology and hydrothermal mineralogy of U. S. Geological Survey Newberry 2 drill core from Newberry Caldera, Oregon: Journal of Geophysical Research, v. 93, no. 9, p. 10,174-10,190.

Kramer, J. C., 1980, Geologic guide to the Modoc Plateau and the Warner Mountains: Sacramento, CA; Geological Society of Sacramento, 156 p.

Lambert, R. S. J. and Goles, G. G., 1992, Newberry Volcano: Sr, Nd and Pb isotopic reservoirs: Geological Society of America Abstracts with Programs, v. 24, no. 5, p. 38.

Langmuir, C. H., Vocke, R. D. Jr., Hanson, G. N., Hart, S. R., 1978, A general mixing equation with applications to icelandic basalts: Earth and Planetary Science Letters, v. 37, p. 380-392.

Lavine, A. and Aalto, K. R., 1997, Morphology of a crater-filling lava lake margin, the Peninsula tuff cone, Lava Beds National Monument, Modoc County, NE

California: Geological Society of America Abstracts with Programs, v. 29, no. 5, p. 24-25.

LeBas, M. J., Le Maitre, R. W., Streckeisen, A., Zanettin, B. A., 1986, A chemical classification of volcanic rocks based on the total alkali-silica diagram: Journal of Petrology, v. 27, no. 3, p. 745-750.

Lee, C. L. and Cummings, M. L., in review, Geology of the Soloman Butte quadrangle, Klamath County, Oregon: Oregon Department of Geology and Mineral Industries GMS-?, scale 1: 24,000.

Leonard, A. R. and Harris, A. B., 1974, Ground water in selected areas in the Klamath Basin, Oregon; State of Oregon, 21 p.

Lienau, P. J. and Lund, J. W., 1993, Groundwater anomalies associated with the Klamath Basin earthquakes of September 20-24, 1993: Geo-Heat Center Quarterly Bulletin, v. 15, no. 2, p. 17-19.

Linneman, S. R., 1990, The petrologic evolution of the Holocene magmatic system of Newberry Volcano, central Oregon [Ph. D. thesis]: University of Wyoming, 293 p.

MacDonald, G. A., 1966, Geology of the Cascade Range and Modoc Plateau: Bulletin-California, Division of Mines and Geology, San Francisco, CA, p. 65-96.

MacLeod, N. S., Sherrod, D. R., Chitwood, L. A., 1982, Geologic map of Newberry Volcano, Deschutes, Klamath, and Lake counties, Oregon, scale 1: 62,500: U. S. Geological Survey Open-File-Report 82-847.

MacLeod, N. S. and Sherrod, D. R., 1985, The magmatic system of Newberry Volcano, Oregon: Open-File-Report - U. S. Geological Survey Open File summary, p. 40-41.

MacLeod, N. S. and Sherrod, D. R., 1988, Geologic evidence for a magma chamber beneath Newberry Volcano, Oregon: Journal of Geophysical Research, v. 93, no. 9, p. 10,067-10,079.

MacLeod, N. S., Sherrod, D. R., Chitwood, L. A., Jensen, R. A., 1995, Geologic map of Newberry Volcano, Deschutes, Klamath, and Lake counties, Oregon: U. S. Geological Survey.

McDonough, W. F. and Sun, S., 1995, The composition of the Earth; Chemical evolution of the mantle: Chemical Geology, v. 120, no. 3-4, p. 223-253.

McKee, E. H. and Duffield, W. A., 1979, Age and volume of basaltic rocks, Modoc County, California: Geological Society of America Abstracts with Programs, v. 11, no. 3, p. 91.

McKee, E. H., Duffield, W. A., Stern, R. J., 1983, Late Miocene and early Pliocene basaltic rocks and their implications for crustal structure, northeastern California and south-central Oregon: Geological Society of America Bulletin, v. 94, p. 292-304.

McKenzie, D. and O'Nions, R. K., 1991, Partial melt distributions from inversion of rare earth element concentrations: Journal of Petrology, v. 32, p. 1021-1091.

Merewether, E. A., 1953, The Geology of the Lower Sprague River Area, Klamath County, Oregon [M. S. thesis]: University of Oregon, 150 p.

Mertzman, S. A. J., 1977, The petrology and geochemistry of the Medicine Lake Volcano, California: Contributions to Mineralogy and Petrology, v. 62, p. 221-247.

Meyers, J. D. and Newcomb, R. C., 1952, Geology and ground water resources of the Swan Lake-Yonna Valleys area, Klamath County, Oregon: Open File Report, U. S. Geological Survey (unnumbered), p. 151.

Miller, M. S., 1988, Mineral resources of the South Warner Contiguous Wilderness Study Area, Modoc County, California, MLA 20-88: Spokane, WA, U. S. Bureau of Mines, Western Field Operations Center, 62 p.

Miyashiro, A., 1975, Volcanic rock series and tectonic setting: Annual Review of Earth and Planetary Sciences, v. 3, p. 251-269.

Montgomery, S. L., 1988, Modoc Plateau; a question of origins: Petroleum Frontiers, v. 5, no. 4, p. 41.

Peacock, S. M. and Leeman, W. P., 1994, Thermal and petrologic evolution of the Cascadia Subduction Zone: Eos, Transactions, American Geophysical Union, v. 75, no. 45, Suppl., p. 621.

Pearce, J. A. and Parkinson, I. J., 1993, Trace element models for mantle melting: application to volcanic arc petrogenesis: Geological Society Special Publication, no. 76, p. 373-403.

Peterson, N. V. and McIntyre, J. R., 1970, The reconnaissance geology and mineral resources of eastern Klamath County and western Lake County, Oregon; Oregon Department of Geology and Mineral Industries Bulletin, 70 p.

Pezzopane, S. K. and Weldon, R. J. II, 1993, Tectonic role of active faulting in central Oregon: Tectonics, v. 12, no. 5, p. 1140-1169.

Prueher, L. M. and McBirney, A. R., 1988, Relations of cinder cones to the magmatic evolution of Mount Mazama, Crater Lake National Park, Oregon; Journal of Volcanology and Geothermal Research, v. 35, p. 253-268.

Sawlan, M. G. and Russell, K. D., 1991, Rhyolite domes, NW-trending faults, gold deposits, and high-alumina basalt in the Devil's Garden, NW Basin and Range; rapid volcanic and structural evolution from 8-6 Ma at Quartz Mountain, south-central Oregon: Geological Society of America Abstracts with Programs, v. 23, no. 2, p. 95.

Schilling, J. G., Zajac, R., Evans, T., Johnston, W., White, J. D., Kingsley, R., 1983, Petrologic and geochemical variations along the Mid-Atlantic Ridge from 27ºN to 73ºN: American Journal of Science, v. 283, p. 510-586.

Schwarzer, R. R. and Rogers, J. J. W., 1974, A worldwide comparison of alkali olivine basalts and their differentiation trends: Earth and Planetary Science Letters, v. 23, p. 286-296.

Shen, Y. and Forsyth, D. W., 1995, Geochemical constraints on initial and final depths of melting beneath mid-ocean ridges: Journal of Geophysical Research, v. 100, p. 2211-2237.

Sherrod, D. R., 1988, Geology, petrology, and volcanic history of a portion of the Cascade Range between latitudes 43º - 44º N, central Oregon, U.S.A. [M. S. thesis]: Oregon State University, 245 p.

Sherrod, D. R. and MacLeod, N. S., 1979, The last eruptions at Newberry Volcano, central Oregon: Geological Society of America Abstracts with Programs, v. 11, no. 3, p. 127.

Sherrod, D. R. and Pickthorn, L. G., 1992, Geologic Map of the west half of the Klamath Falls 1º by 2º Quadrangle, south-central Oregon: U.S. Geological Survey, scale 1:250,000.

Sisson, T. W. and Grove, T. L., 1993, Experimental investigations of the role of H_2O in calc-alkaline differentiation and subduction zone magmatism: Contributions to Mineralogy and Petrology, v. 113, p. 143-166.

Walker, G. W. and MacLeod, N. S., 1991, Geologic map of Oregon: U. S. Geological Survey, scale 1:500,000.

Wiley, T., in press, Geologic Map of the Fort Klamath quadrangle, Klamath County, Oregon: Oregon Department of Geology and Mineral Industries GMS-?, scale 1: 24,000.

Williams, H., 1942, The geology of Crater Lake National Park, Oregon: Carnegie Institute of Washington, Publication no. 540, p. 162.

Williams, H., Turner, F. J., Gilbert, C. M., 1954, Petrography, An Introduction to the Study of Rocks in Thin Sections: San Francisco, CA, W. H. Freeman and Company, 406 p.

Wilson, M., 1989, Igneous Petrogenesis: A Global Tectonic Approach: London, England, Academic Division of Unwin Hyman Ltd., 466 p.

Wood, C. A. and Kienle, J., 1990, Volcanoes of North America: United States and Canada, Cambridge University Press, 354 p.

Young, S. R., 1990, Physical volcanology of Holocene airfall deposits from Mt. Mazama, Crater Lake, Oregon [Ph. D. thesis]: University of Lancaster, 326 p.

Zdanowicz, C. M., Zielinski, G. A., Germani, M. S., 1999, Mount Mazama eruption: Calendrical age verified and atmospheric impact assessed: Geology, v. 27, no. 7, p. 621-624.